Myelinated axons and functional blood vessels populate mechanically compliant rGO foams in chronic cervical spinal cord hemisected rats

Ana Domínguez-Bajo, Ankor González-Mayorga, Carlos R. Guerrero, F. Javier Palomares, Ricardo García, Elisa López-Dolado, and María Concepción Serrano*

A. Domínguez-Bajo, C. R. Guerrero, Dr. F. J. Palomares, Prof. R. García, Dr. M. C. Serrano
Materials Science Factory, Instituto de Ciencia de Materiales de Madrid (ICMM), Consejo Superior de Investigaciones Científicas (CSIC), Calle Sor Juana Inés de la Cruz 3, Madrid, 28049, Spain
E-mail: mc.terradas@csic.es

A. González-Mayorga, E. López-Dolado
Laboratory of Interfaces for Neural Repair, Hospital Nacional de Parapléjicos, SESCAM, Finca la Peraleda s/n, Toledo, 45071, Spain

E. López-Dolado
Research Unit of "Design and development of biomaterials for neural regeneration", HNP-SESCAM, Joint Research Unit with CSIC, Spain

Neural diseases at the central nervous system including spinal cord injury (SCI) remain therapeutic challenges. Graphene-based materials are being delineated as alternative tools for neural repair. Herein, the pro-regenerative ability of reduced graphene oxide (rGO) scaffolds to support pivotal features of neural repair at 4 months after SCI is demonstrated. 3D randomly porous foams have been prepared to be mechanically compliant with neural cells and tissues (Young's modulus of 1.3 ± 1.0 kPa) and softer than the majority of biomaterials investigated for SCI to date. After implantation, the significant increase in Young's modulus caused by massive cell/protein infiltration does not alter the mechanical performance of the contralateral spinal cord but provides mechanical stability to the lesion. These aerogels appear fully vascularized and

populated with neurites, some of them being myelinated excitatory axons. Magnetic resonance image studies demonstrate that the scaffolds significantly reduce the surface of perilesional damage with respect to rats without implants and cause no compressive damage in the contralateral hemicord and rostral/caudal regions. The rGO implants do not either alter the rat spontaneous behavior or induce toxicity in major organs. Finally, preliminary data suggest hints of rGO degradation at the injured spinal cord for the first time.

1. Introduction

Since the very first attempts with neurons in 2011,[1] it seems more and more reliable that graphene-based materials (GBMs) might provide alternative therapeutic approaches for neural repair.[2] To date, GBMs have been already proved *in vitro* to stimulate neural differentiation from neural and non-neural progenitor cells,[1,3] to potentiate the sprouting and outgrowth of neurites,[4] to stimulate electrical signaling in neural networks,[5] to reshape neuronal synapses functioning,[6] and to increase neuronal firing by tuning the distribution of extracellular ions,[7] among others. As part of 3D scaffolds, they have also shown positive responses when implanted in the peripheral nervous tissue aiming nerve repair.[8] In the central nervous system (CNS), reduced graphene oxide (rGO) nanosheets behave as permissive materials for neurogenesis when implanted in the olfactory bulb.[9] Interestingly, recent studies have proved the preferential interaction of graphene with cholesterol, potentiating neurotransmission by increasing the number, release probability and recycling rate of synaptic vesicles.[10] Although toxicity concerns are still on stage until the behavior of GBMs in biological systems becomes completely clear,[11] it seems reasonable the existence of a range of

doses, sizes and shapes that could be safely used.[12] Concerns on the biodegradability of these materials also persist, although evidences of their capacity to undergo biologically-mediated degradative processes *in vitro* start to appear.[13-15] No structural changes or degradation were observed when tested in diverse simulated human gastrointestinal media *ex vivo*.[16]

Scars at the CNS are mainly formed from glial cells (*e.g.,* astrocytes and NG2-glia) accompanied by some non-neural cells such as pericytes and meningeal cells,[17] along with collagen and other extracellular matrix components. Importantly, and contrary to scars in other tissues, the CNS tissue significantly softens after injury, both at the neocortex and the spinal cord, as demonstrated by atomic force microscopy (AFM).[18] In this sense, extensive work has already demonstrated that the mechanical properties of the environment play a pivotal role in cell and tissue responses. For instance, neural stem cells fate can be directed by the stiffness of the substrate (preferentially differentiating into neurons in stiffer substrates).[19] Moreover, neurites of dorsal root ganglion cells grow longer on stiffer substrates,[20] and spinal cord astrocytes adapt their morphology to the mechanical properties of the substrate.[21] Thus, it seems reasonable to hypothesize that the reduced ability of neurons to regrow in CNS injuries could be partially associated with changes in the mechanical properties at the lesion site.[18]

Spinal cord injury (SCI) continues to be an enormous challenge for scientists and clinicians as there is not an effective therapy to date. Approximately 66 % of the traumatic SCIs in humans occur in the cervical region and 70 % of them are incomplete[22] and lead to chronic sensory-motor upper limb deficits that hinder self-care, independence in the activities of daily living and arm use. Most of these deficits can be attributed to the tracts axotomy, which massively disrupt the descending inputs

in all the spinal segments caudal to the lesion epicenter. However, segmental neuronal death also contributes in a great extent to the chronic upper limb deficits in humans,[23] or its homologous forelimb in rats.[24] While the acute SCI phase is characterized by neuronal and glial death, axonal and vascular damage, release of inhibitory neurotransmitters, and ionic disruption, the chronic phase is defined by the neurological deficits stabilization.[25] Therefore, it is of great importance to analyze the chronic stage to determine the relative contribution of any proposed therapeutic intervention *versus* the spontaneous recovery to the functional improvements found. In this context, multidisciplinary efforts are providing encouraging results toward restoring lost functions after SCI,[26,27] including biomaterials.[28-30] In this scenario, recent biomaterials tested range from organic polymers[31,32] to macromolecules including chitosan,[33] and carbon nanotubes,[34,35] to cite a few. Alternatively, in our laboratory, we pioneered the exploration of hierarchically channelled 3D rGO scaffolds as advanced platforms to support neural repair after SCI.[36,37] Herein, we demonstrate how randomly porous 3D rGO foams enhance reparative neural responses in long-term chronic hemisected rats (4 months) by means of a multidisciplinary approach including the use of AFM, magnetic resonance imaging (MRI), behavioural tests, standard histological techniques, immunofluorescence studies, confocal laser scanning microscopy, and transmission electron microscopy. As the CNS is composed of very soft cells with mechanical features similar to elastic solids,[38] these rGO foams are thought to provide a soft scaffolding structure containing mechanical clues in agreement with those of native neural tissues.

2. Results

2.1. Fabrication and characterization of mechanically compliant rGO foams

Graphene oxide (GO) slurry used for scaffold fabrication was morphologically characterized by TEM. GO was found to form abundant micron-sized sheets with several layers piled-up (**Figure 1**a). These GO micro-sheets were then dispersed in an aqueous solution and forced to build-up in a 3D structure by simple freeze-casting at -80 ºC. After ice removal by freeze-drying and a subsequent thermal treatment at 200 ºC for 30 min for GO reduction, rGO micro-sheets assembled into a soft 3D structure with random porosity as characterized by scanning electron microscopy (SEM) (Figure 1b). Interestingly, these foams had partition walls relatively flat and smooth, with transversal sections on the size of hundreds of nm. The high-degree porosity of the resulting structures (43.87 ± 3.46 % of porosity and 31.88 ± 19.43 μm of pore size) enable tissue infiltration when implanted. These porous 3D rGO scaffolds, conversely to those previously explored by our group,[36,37] avoided the need of hierarchical channels which are scarcely respected by the ingrown tissue when implanted and prevent the necessary transversal regrowth of neurites for propiospinal reconnection.

Comparative X-ray photoelectron spectroscopy (XPS) studies of GO slurry, GO scaffolds and rGO scaffolds confirmed a significant increase in the reduction degree of the samples, accompanied by a decrease of their correspondent O/C ratio from 0.84 to 0.28 % (Figure 1c and **Table S1**). This fact is in line with the signal in the energy region where the photoelectrons from C-OH and O-C-O groups are emitted, whose intensity also decreased with the O1s signal. The rGO and GO scaffolds spectra are mainly governed by a high intensity component with asymmetric line shape whose parameter values (peak position and full width half maximum) were obtained by fitting the C1s

signal from the HOPG reference sample. Therefore, its origin can be certainly ascribed to sp^2 bonding. This major asymmetric peak is followed by a symmetric one of much lower intensity (~15 and 10 %, respectively) shifted 0.85 eV towards higher binding energy. On the one hand, this latter component might be assigned to the presence of a small amount of carbon atoms with sp^3 nature due to the observed chemical shift, which is in good agreement to reported values. However, on the other hand, it might also be attributed to disordered regions with sp^2 defect-like bonding expected in the outer surface of the sample. Conversely, in the GO slurry, C-C emission is fitted with a single symmetric peak representative of its oxide nature. There also exist two symmetric contributions related to carbon atoms bound to oxygen at the energy shifted values reported in the literature for hydroxyl C-OH, carbonyl C-O and carboxyl C=O groups.[39] Finally, the feature at binding energy of 290.8 eV (broader than any of the previous ones), is clearly associated to the characteristic π-π* shake-up transition consistent with a majority existence of sp^2 configurations in the sample.[39]

The mechanical properties of the environment are essential regulators of the biological responses. In this sense, different cells and tissues are characterized by specific ranges of elastic properties, thus making mechanical compliance a pivotal requisite for tissue engineering applications. The elastic response of the rGO scaffolds prepared was quantified by their Young's modulus, *E*, and compared with that from neural cells and spinal cord tissue (Figure 1d). Values were obtained from AFM-based indentation experiments (**Figure S1** and **S2**).[40,41] The macroscopic softness of these rGO scaffolds was confirmed by their Young's moduli (1326 ± 1004 Pa). Comparatively, single cortical neurons cultured *in vitro* were characterized by a *ca.* 3-fold lower Young's modulus value of 417 ± 106 Pa (p < 0.001), which was itself significantly higher than the values obtained on white and grey matter regions from

fresh spinal cord slices (97 ± 69 and 275 ± 99 Pa, respectively; p < 0.001). These values

for spinal cord tissue are in range with those previously reported for the spinal cord (177

and 420 Pa, respectively) and the rat cortical tissue (50 to 500 Pa).[18] When compared

to the elastic response of paraformaldehyde-fixed spinal cord tissue, the Young's

modulus values of both white and grey matters significantly increased with respect to

their fresh counterparts (296 ± 211 and 1324 ± 1202 Pa, respectively; p < 0.001), as

expected from chemically cross-linked tissues,[42] but similar to those obtained for the

rGO scaffold in the case of grey matter areas (p > 0.999). In any case, the softer nature

of the white matter is likely related to its higher content of myelin and other lipid-

containing components.[18]

Interestingly, somata of pyramidal neurons display elastic modulus between 480

Pa at 30 Hz and 970 Pa at 200 Hz, while values in astrocytes, even though being softer,

reached 300 Pa at 30 Hz and 520 Pa at 200 Hz.[38] Somata of retinal neurons reached

values as high as 1590 Pa at 200 Hz. In other tissues, for instance, fibroblasts displayed

an elastic storage value as high as ~5 kPa at 0.1-4.0 Hz,[41] dramatically higher than the

elastic modulus of our rGO scaffolds. Moreover, these rGO foams are significantly

softer than most of the biomaterials implanted at the injured spinal cord to date, even

hydrogels, which account for an additional major drawback that is their fast *in situ*

degradation. Some examples include porous methacrylate hydrogels (2.9 ± 0.4 kPa

perpendicular to pores and 6.7 ± 1.8 kPa along pores),[43] cholesterol-modified

superporous methacrylate hydrogels (10.1 ± 1.8 kPa),[44] protein-functionalized

methacrylate scaffolds (263 ± 13 kPa),[45] ordered porous polycaprolactone scaffolds

(2.1 MPa),[46] and polycaprolactone/gellan gum blends (79.7 ± 7.56 kPa),[47] to cite a

few. Even though all these biomaterials have reported favorable regenerative responses

such as axon growth at the injured spinal cord, no data exist on the potential mechanical distress caused by their mechanical mismatch with the neural tissues.

2.2. Preservation of spontaneous behaviour features in chronic rGO-implanted rats

We then proceeded to implant these 3D rGO scaffolds in acute C6 hemisected rats, immediately after removal of the right C6 hemicord. A consistent anatomo-functional spinal cord correlation has been extensively reported to correlate the specific control of every muscle with each particular spinal segment. This fine topographical organization can predict the deficits according to the level of the injury.[48] As expected, this SCI model caused a significant initial impairment of the ipsilateral forelimb and both hindlimbs. Later on, while both hindlimbs but mainly the left one progressively recovered to functional levels, the ipsilateral impaired forelimb remained damaged for the 4-month period analysed.[49] In order to evaluate the degree of focal functional affectation and its progression over time, two tests involving the specific use of forelimbs and characteristic of the spontaneous rat behaviour were selected: grooming and forelimb asymmetry tests. These tests are quite comparable to the clinical tools used to evaluate functional independence for daily living activities in SCI patients.[50] Interestingly, despite the impairments caused by the lesion, animals showed no significant differences in the time spent at either grooming (p = 0.768) or naturally exploring the environment (p = 0.903) once the injury-induced spinal cord shock was resolved (**Figure S3**). In all groups, the left forepaw (LFP) retrieved the maximum score (*i.e.,* 5), while injured animals displayed a marked but not statistically significant impartment in the use of the right forepaw (RFP) at 120 days post-injury (DPI) (3.83 ± 0.98 for injured rats without scaffolds – *I rats*, 3.20 ± 1.30 for *rGO* and 5.00 ± 0.00 for

control rats; p = 0.432 and p = 113, respectively to control) (**Figure 2**a). The functional RFP impairment was only statistically significant at 10 DPI (p = 0.024). We next quantified the rate of the different grooming positions reached by both forelimbs, with special attention to positions 3 to 5 and back side (Figure 2b). All injured animals groomed significantly less intensively with the RFP at the most challenging positions (5 and back side) than control rats (p = 0.002 and p = 0.024, respectively to control). Importantly, rats carrying rGO scaffolds were unable to reach positions further than the eyes area (*i.e.,* position 3) at earlier time points (10 and 30 DPI). In any case, animals retained the ability to throw the RFP to reach positions 3 and 4, but typically failed to lift it high enough to reach position 5 or further and make contact with the body surface (Figure 2d and 2e). Position 5 and the right back side were scarcely explored during the grooming time (Figure 2f and 2g). To compensate for RFP deficits, all injured animals overused the LFP to reach position 3, although this difference was not statistically significant (p = 0.146).

Asymmetry tests revealed that both groups of injured animals avoided leaning on their RFP, solving the necessity of body support by almost exclusively resting on the open LFP palm (Figure 2h and 2i). In these rats, the LFP use was therefore significantly prioritized over the use of both paws typical of control animals (p < 0.001; Figure 2j). No statistically significant differences were found on the frequency of stand-ups among groups (p = 0.272), neither on the use of the RFP (p = 0.164). All together, the acute and chronic functional impairments caused by the unilateral hemisection practiced in this study were in agreement with previous findings in cervical SCI.[49,51] Moreover, minor motor behaviour improvements might have also occurred, as studies regarding upper limbs in humans have evidenced that clinical tests may fail discriminating subtle functional changes.[52]

2.3. Outstanding MRI findings of 4-months rGO implants

A clinically inspired MRI protocol was used to analyse the whole cervical spinal cord enlargement (*i.e.,* metameres between the caudal part of C4 and the caudal part of T1) in an attempt to: (1) have a "contextualized" morphological vision of the lesion epicenter with and without implants and (2) search for radiological signs of damage, along all the metameres responsible for the rat forelimb functions, not directly caused by the hemisection, to accurately interpret the behavioural test results. In all animals, the lesion epicenter was located in the right C6 hemicord and affected it almost entirely (**Figure 3**a). Its dimensions were significantly higher in rats receiving rGO scaffolds, both as measured as the mean maximum transverse diameter (2.4 ± 0.06 mm in rGO and 1.06 ± 0.14 mm in *I* rats; p = 0.008) and the mean lesion volume (26.41 ± 3.24 mm^3 in rGO and 6.29 ± 1.28 mm^3 in *I* rats; p = 0.008) (Figure 3b). No radiological signs of either syringomyelia or hematomyelia were found in any injured animals. Slight left displacements relative to the midline were found in the coronal sections of rGO rats (0.26 ± 0.11 mm), suggesting a possible "mass effect" of the scaffold (Figure 3c). However, no signs of compressive damage were found in either the contralateral hemicord or the rostral/caudal regions. Differential features in the MRI signal intensity at the interface zone, eventually related to a foreign body reaction, could not be identified. The interface volume was indirectly quantified in the rGO group by subtracting the volume of the scaffold itself from the total volume of the whole lesion area. Interestingly, the mean volume of the interface was not higher than the volume of the lesion itself in the *I* group (5.30 ± 3.25 mm^3 versus 6.29 ± 1.28 mm^3, respectively; p = 0.784). Therefore, most of the lesion volume increment in rGO rats was primarily due to the scaffold itself but not to an increment of the surrounding interface.

Areas of perilesional damage were always identified in the ipsilateral side of the spinal cord in both groups (Figure 3c), both above or below the lesion, at a similar distance from the lesion epicenter (2.64 ± 0.85 mm in I rats and 1.92 ± 0.53 mm in rGO rats; $p = 0.566$) and with a similar extension along the coronal sections (2.76 ± 0.38 mm in I rats and 1.89 ± 0.72 mm in rGO; $p = 0.286$). Nevertheless, the mean damage surface was significantly larger in rats without rGO scaffolds (0.95 ± 0.29 mm^2 in I and 0.18 ± 0.03 mm^2 in rGO; $p = 0.005$), corresponding to hyper-intense areas suggestive of gliosis.[53,54] Finally, a similar mean MRI signal intensity was measured in both groups (1.70 ± 0.26 in I and 1.48 ± 0.49 in rGO; $p = 0.102$), thus suggesting the same type of phenomenon taking place in both injured rats but being more dramatic in those animals without rGO implants.

2.4. rGO foams promote collagen deposition and provide structural support to the lesion

Contrary to lesions at the brain and likely related to its softer nature, injuries at the spinal cord typically result in irregular and diffuse boundaries with a varying degree of tissue damage among animals.[18] This softening is also significant outside of the lesion site. These features add both uncertainty in defining the size/location of the lesion and an extensive variability to the data. In our case, this effect was especially evident in the case of injured rats without rGO scaffolds. Conversely, the presence of the rGO scaffold clearly assisted the structural stabilization of the lesion site and diminished these phenomena.

By using a conventional Masson's trichrome staining, we identified the infiltration of both cells and collagen fibers in both groups (**Figure S4**a), although largely more abundant within the rGO foams implanted. More importantly, the chronic evolution of the injury revealed significant differences in the area occupied by cavities,

with a 29.4 ± 10.3 % of empty areas in *I* rats and as low as 5.6 ± 2.8 % in rGO animals as quantified from histological sections (p = 0.023). When visualized by TEM (Figure S4b), lesion areas holding rGO foams were found highly compact, with rare free space but abundant cells and deposited collagen fibers. rGO sheets forming the foam walls were clearly identifiable. On the contrary, the injury site in *I* rats was characterized by profuse empty space and disorganized tissue elements. When estimated from TEM images at low magnification (2,000X), a significantly different distribution of grey-scale pixels was detected between groups, with a predominant peak in the whitish region corresponding to pure resin without biological content in rats without implants (Figure S4c; maximum peaks location: pixels 78 and 163 for *rGO* and 158 and 224 for *I* rats, statistically significant differences between groups at pixels 3-34, 90-195, and 205-254, at least p < 0.05).

2.5. rGO foams transmit mechanically compliant signals to the injured spinal cord tissue

AFM-indentation measurements were then carried out on the spinal cord tissue containing the rGO scaffolds implanted for 4 months (Figure 1e). Young's modulus values are provided for the main regions of the sample as depicted in the scheme (Figure 1f). As expected from damage in the CNS,[18] the interface tissue showed a significantly lower Young's modulus (54 ± 29 Pa; p < 0.001). However, the lesion site carrying the rGO scaffolds displayed the significantly highest Young's modulus (3624 ± 2664 Pa; p < 0.001), even when compared to the rGO scaffolds before implantation (1326 ± 1004 Pa), likely due to collagen deposition and massive cell infiltration of the foam. Nonetheless, and importantly, this decrease in the elasticity of the right hemicord holding the scaffold was not transmitted to the left counterpart spinal tissue, as its

elastic response was found in range with the one found in the fresh control spinal cord tissue (237 ± 66 and 225 ± 109 Pa, respectively; p = 0.366; control spinal cord tissue calculated as the average of the values for grey and white matters).

2.6. Reduction in macrophages and vimentin^{+} cells infiltrating rGO foams

The first observable consequence at the cellular level of the lesion practised was a significant increase in cell density both at the lesion epicentre and, to a lower extent, in its caudal and rostral interfaces in all injured animals as demonstrated by Hoechst staining (**Figure S5**; p < 0.001). Most of these lesion-infiltrating cells might have been recruited by the release of chemotactic messengers from blood vessels in the surroundings but also resulted from the proliferation of local cells at the injured spinal cord at early times of the lesion. Indeed, we already observed significant cell colonization of comparable rGO scaffolds as early as 10 DPI,[36] which were maintained at 30 DPI.[37] When compared with injured rats without scaffolds, two major significant differences were identified: (1) The presence of the rGO scaffold significantly decreased cell density at the lesion site (p < 0.001) and (2) in the absence of the scaffold (*I* rats), cell density slightly increased in perilesional areas at 1-2 mm from the lesion border (PL12) with respect to their correspondent left hemicord (LH, p = 0.023).

We next investigated the presence of specific markers for major features of native and injured neural tissue by immunostaining (**Figure 4**). Control and *I* rats were processed and analysed in parallel with *rGO* rats for comparisons (**Figure S6**). First, neural components were visualized by labelling for map-2 and tau, two major cytoskeleton proteins expressed by neurons. No statistically significant differences were found in either LH or PL12 (p = 0.589 for map-2 and p = 0.051 for tau at LH; p = 0.347 for map-2 and p = 0.741 for tau at PL12). However, the interface tissue, both rostral and

caudally (RIF and CIF, respectively), experienced a significant decrease in the presence of map2 and tau in *rGO* rats (p < 0.02 for CIF and RIF with respect to map-2 LH; p < 0.009 for CIF and RIF with respect to tau LH). These differences were also evidenced in *I* rats, except for the presence of tau at RIF which remained similar to the LH (p < 0.003 for CIF and RIF with respect to map-2 LH; p = 0.004 for CIF and p = 0.069 for RIF with respect to tau LH). In any case, the presence of both proteins was comparable in both regions for both treatment groups (map-2: p = 0.613 for CIF and p = 0.512 for RIF; tau: p = 0.124 for CIF and p = 0.510 for RIF). However, at the lesion site, all injured animals experienced a dramatic reduction of both neural markers when compared to LH (p < 0.001). Nonetheless, the presence of limited but detectable positive labelling at the lesion site for these two markers deserved further investigation as will be explained later.

The presence of activated astrocytes labelled as GFAP$^+$ cells was significantly restricted to the interface area (p < 0.001 with respect to LH, PL12 and lesion areas for both CIF and RIF), without evidences of significant penetration into the rGO foam (p = 0.081 with respect to LH). Conversely, a significant amount of GFAP$^+$ cells were found at the lesion site in *I* rats (p = 0.002). ED1$^+$ cells accounting for macrophages were also significantly abundant at both CIF and RIF in both *I* and *rGO* rats (p < 0.003 with respect to LH and PL12). The amount of macrophages did not differ at CIF between *I* and *rGO* rats (p = 0.095), but did at PL12 (p = 0.003) and RIF (p = 0.001). More importantly, the presence of the rGO implants dramatically reduced the amount of macrophages invading the lesion site with respect to *I* rats (p < 0.001), being just slightly above values found at the LH (p = 0.042).

The interface tissue in both *I* and *rGO* rats was also characterized by the significant presence of cells positive for vimentin and PDGFRβ (p ≤ 0.001 for both CIF

and RIF with respect to LH and PL12). Vimentin, but not PDGFRβ, was significantly less abundant at the lesion site than at the interface (vimentin: $p = 0.027$ with respect to CIF and $p = 0.010$ with respect to RIF; PDGFRβ: $p = 0.764$ with respect to CIF and $p = 0.585$ with respect to RIF). There were no significant differences attributed to the presence of the rGO foam for PDGFRβ in any of the areas under study ($p > 0.05$), but there were for vimentin at both interfaces and the lesion site ($p < 0.002$). In injured animals without rGO scaffolds, the abundance of these markers was only significantly reduced with respect to the lesion site in the case of RIF for vimentin (vimentin: $p = 0.266$ with respect to CIF and $p = 0.049$ with respect to RIF; PDGFRβ: $p = 0.906$ with respect to CIF and $p = 0.502$ with respect to RIF). Remarkably, at the lesion site, vimentin but not PDGFRβ was significantly reduced by the presence of rGO (vimentin: $p < 0.001$; PDGFRβ: $p = 0.309$). We hypothesize that cells positive for these two markers might be having a positive role at the lesion site, as vimentin is considered a marker of immature glial cells and new-born neural stem cells[55] and PDGFRβ is expressed by highly proliferative type A pericytes, essential to regain tissue integrity after SCI.[17] In any of the cases, LH in animals carrying rGO foams showed no statistically significant differences when compared with undamaged grey matter areas in control rats except for a slight decrease in GFAP ($p = 0.001$).

2.7. Ingrowth of myelinated vGlut2[+] axons within rGO scaffolds

To further elucidate the presence of map2[+] and tau[+] elements within the rGO foams, two additional markers were investigated: β-III tubulin and SMI311, specifically binding to proteins contained in cytoskeleton microtubules and neurofilaments, respectively. Interestingly, positive staining for both markers was found in all five animals carrying rGO scaffolds dedicated to these studies (**Figure 5**a). 3D-plots more

clearly illustrate the significant colonization of the scaffold by β-III tubulin[+] and

SMI311[+] neurites (Figure 5b). A representative PL12 region was plotted for comparison.

Curiously, when images for both markers were merged, elements uniquely stained for

either β-III tubulin or SMI311were identified (Figure 5c), as well as double-stained

neurites. When quantified, neurites re-growth within the rGO foams accounted for 5.42

± 1.75 mm per μm^2 of scaffold for β-III tubulin and 3.71 ± 2.57 for SMI311. The

predominant expression of β-III tubulin against other neurite markers is not surprising

as, during mammalian and avian development, this protein is considered the earliest

neuron-associated cytoskeletal marker.[56,57] Importantly, its expression is maintained in

mature neurons and confers microtubules a more dynamic nature, likely related to

neurites in the process of development and growth.[58] The presence of both markers at

the LH and PL12 was not significantly affected by the rGO implants (**Figure S7**; p >

0.05). However, the lesion reduced, although not significantly, the presence of both

proteins at the interface (p > 0.05), both rostral and caudally, in a similar magnitude to

that found in injured animals not carrying rGO foams (p > 0.05).

We next investigated the chemical nature of these new neurites by looking at

specific neurotransmitters. The presence of vesicular glutamate transporter 2 (Vglut2)

was used for identifying excitatory glutamatergic fibers, tyrosine hydroxylase for

excitatory dopaminergic fibers and serotonin for inhibitory serotoninergic ones (Figure

5d). Neurites growing within the rGO foams were found predominantly positive for

Vglut2. Tyrosine hydroxylase, if present, was negligible. Regarding serotonin, although

a positive labelling was observed within the scaffold, neither the morphology of the

staining nor the association with β-III tubulin[+] neurites reflected mature serotonin fibers,

so we attributed this finding to either non-specific binding sites for the antibody or early

immature serotoninergic fibers. Importantly, when the presence of all three

neurotransmitters systems was studied in PL12 and LH, no statistically significant changes were detected in comparison to control rats in any case (Figure 5e; Vglut2: 107.8 ± 17.0 % and 120.1 ± 31.9 %, p = 0.467; TH: 82.5 ± 65.9 % and 72.6 ± 57.5 %, p = 0.746; 5-HT: 128.8 ± 72.0 % and 115.4 ± 45.6 %, p = 0.713, respectively for PL12 and LH). Finally, detailed morphological TEM analysis of the ingrown neurites within the rGO foams revealed the existence of organized multi-layer myelin coatings in some of these neural elements (Figure 5f).

Functional recovery in incomplete SCI is associated to neuroanatomical plasticity processes, which comprise sprouting of spared fibers (compensatory plasticity), sprouting and regrowth of severed fibers (regenerative plasticity) and plastic adaptations in both supraspinal and intraspinal neural circuits.[59] Specifically, spared reticulospinal fibers are able to initiate compensatory adaptations by spontaneous sprouting below the lesion at the lower thoracic cord.[60] Besides, propiospinal neurons also display high intrinsic potential for neuroanatomical adaptations,[61] participating in the formation of propiospinal detour pathways.[62] They are thought to participate in the compensatory mechanisms for motor function restoration in forelimbs, especially in the case of finger function.[63] The newly-grown axons found within the rGO scaffolds might have origin in brainstem nuclei, more largely devoted to forelimb rather than hindlimb motor neurons.[64] The abundance of Vglut2$^+$ labelling could be in agreement with this brainstem nuclei origin for those, as glutamate (in particular the Vglut2 system) is the predominant transmitter pathway in the brainstem neurons responsible for excitatory motor commands.[65] These results support the hypothesis of rGO foams reinforcing intrinsic plastic adaptations in preexisting reticulo-propiospinal connections after cervical injuries.

2.8. Formation of new functional microvessels within rGO implants

As blood supply is essential for tissue repair and maintenance and the absence of blood supply is known as one of the major limitations after SCI,[30] we then specifically investigated the abundance of blood vessels within and around the implanted rGO foams by analysing two specific proteins: (1) Reca-1, as a marker of mature vascular endothelial cells, and (2) laminin, as a major component of the basal lamina in vasculature (**Figure 6**). Importantly, a significant amount of Reca-1 was detected within the rGO foams, thus demonstrating the existence of new small-sized blood vessels (*i.e.,* microvessels) likely formed from pre-existing ones at the interface (angiogenesis). Specifically, an average of 109.47 ± 19.43 sectioned vascular structures per mm^2 of scaffold, with an area of $1.02 \pm 0.55 \cdot 10^4$ μm^2 per mm^2 and a diameter of 10.16 ± 6.21 μm were colonizing the interior areas of the scaffold. Although the number of vascular structures was significantly inferior to that found in control grey matter (284.20 ± 41.21; $p < 0.001$), their diameter was similar (9.07 ± 6.34 μm; $p = 0.202$). Interestingly, the area positively stained for Reca-1 did not significantly vary with respect to the control grey matter at any other location including LH, PL12, CIF, and RIF ($p > 0.05$).

When focused on laminin, a slight but not significant increase of this protein was found within the scaffold and PL12 in comparison to the LH, with an area of positive staining of 0.63 ± 1.14 and 0.58 ± 1.06 %, respectively ($p > 0.05$). However, laminin at the interface tissue around the scaffold dramatically augmented ($p \leq 0.002$ for both CIF and RIF with respect to rGO LH), likely serving to guide the new blood vessels to the foam. In this sense, the augmentation in extracellular matrix components including laminin, mainly associated to basal laminae, are known to upregulate after injury,[66] likely related to the destruction of blood vessels caused by the lesion.[18] As RIF experienced a more remarkable increase in laminin than CIF ($p = 0.001$), we

hypothesize a preferential origin of blood vessels from pre-existing ones rostrally located to the scaffold. Laminin expression in *I* rats was markedly higher than on *rGO* rats, although heterogeneous, both around and inside the lesion site (p $\leq$ 0.001). Conversely to rGO-implanted rats, the augmentation of laminin inside the lesion in *I* animals was similar to that found at the interfaces (p > 0.05) and significantly higher than at the correspondent LH (p < 0.001). Both collagen and laminin, identified in the lesion site in rGO rats, are likely driving new microvessels from pre-existing ones to grow throughout the lesion site. This angiogenic phenomenon and subsequent vascular remodeling is of essential relevance for neural repair at the damaged CNS, as recently demonstrated in the brain for hyaluronic acid hydrogels implanted after stroke.[67]

Detailed analysis by TEM demonstrated small-sized vascular elements (mainly capillary but also some terminal arterioles and venules based on size and wall structure), adequately structured within the rGO foams and containing easily identifiable endothelial cells and supportive pericytes around them (Figure 6c). Moreover, it revealed the presence of blood components inside these vascular elements invading the 3D rGO foam (Figure 6d), thus confirming their functioning as blood suppliers to the interior areas of the scaffold. This significant angiogenesis is hypothesized to play an essential role in the neurite regrowth found, in agreement with recent findings after stroke.[67]

2.9. Insights of rGO foam degradation after 4 months in the injured spinal cord

Biodegradation of implantable devices is an attractive feature frequently pursued.[68] Regarding GBMs, recent work with human myeloperoxidase and degranulating human neutrophils point out towards graphene not to be biopersistent.[14] Despite this progress, GBMs degradation in *in vivo* scenarios continues to be poorly understood, with no

reports to date demonstrating any insights of graphene degradation when implanted at the CNS. In this study, TEM was used to carefully identify any degradative features in the rGO foams implanted. High-magnification TEM images first evidenced qualitative changes in the degree of compaction of rGO sheets on the foam walls (**Figure 7**a; 300,000X). Comparisons among rGO foams before and after progressive times of implantation (*i.e.,* 10, 30 and 120 days) revealed a dramatic and significant increase of the thickness of the foam walls (rGO: 84.1 ± 35.6 nm; rGO-10 DPI: 90.2 ± 46.3 nm, $p = 0.789$ with respect to rGO; rGO-30 DPI: 108.4 ± 51.5 nm, $p = 0.005$ with respect to rGO and $p = 0.097$ with respect to rGO-10 DPI; rGO-120 DPI: 138.0 ± 54.6 nm, $p < 0.001$ with respect to rGO, $p < 0.001$ with respect to rGO-10 DPI and $p = 0.004$ with respect to rGO-30 DPI; Figure 7b), accompanied by a clear fading of their colour intensity. Individualized small fragments of rGO sheets were even visible in the surroundings of the walls (red asterisks). When estimated as the variation in colour (Figure 7c), significant changes in the distribution of grey-scale pixels were observed with the time of implantation (maximum peaks location: 229 for rGO, 221 for rGO-10DPI, 206 for rGO-30DPI, and 202 for rGO-120DPI; statistically significant differences among groups at pixels 85-200 and 215-250, at least $p < 0.05$). The observed shift of black pixels to lighter values is attributed to the progressive disassembly of rGO sheets in the foams, while the shift of white ones to darker pixels correlates with an increase in the degree of tissue ingrowth in the foam. Both shifts were accompanied by an expected increase of intermediate grey values. Besides changes in the scaffold structure, rGO fragments were frequently found intracellularly. Hints of attempts of internalization by phagocytosis-like mechanisms were noticed (Figure 7d). Internalized rGO was sometimes included in intracellular compartments (Figure 7e), or directly in contact with cytoplasmic components (Figure 7f and 7g). Disassembly of

rGO sheets was also noticed within cells (Figure 7h). Degradative actions by enzymes and phagocytic immune cells might be pivotal for rGO sheets biodegradation.[14] Importantly, mechanisms of cellular uptake for graphene nanomaterials remain unclear. Previous *in vitro* findings have evidenced the entrance of 350 nm graphene flakes by active filopodia of macrophages and larger ones (2 μm) directly trespassing cell membranes perpendicularly.[69] In a different work, 500 nm-sized GO flakes entered by clathrin-mediated endocytosis, while larger ones (1 μm) underwent phagocytosis in C2C12 mouse mesenchymal stem cells *in vitro*.[70]

2.10. Absence of toxicity insights in major organs

As previous work with GBMs has demonstrated accumulation and eventual granuloma formation in liver, spleen and lungs,[71-73] we then inspected major organs for toxic effects (**Figure S8**). Although scaffold implantation takes place at the injured spinal cord, the degradation features found could drive fragments of our rGO scaffolds to get into the blood stream. Anatomophatological studies revealed no signs of either macroscopic or microscopic organ damage in any of the tissues analysed (*i.e.,* kidney, liver, lung, spleen) at this time point. Respective organ-specific cells in all cases were found morphologically identical to those of control rats by careful hematoxylin/eosin staining and TEM inspection. This absence of organ toxicity is not surprising as the dose used in our case (250 μg per rat, equivalent to ~700 μg Kg^{-1}) was largely below that found toxic by others (400 μg per animal in mice,[71] 10 mg kg^{-1} in mice/rats,[72] and 1-10 mg Kg^{-1} in mice[73]) thus supporting the hypothesis of a dose-dependence toxicity already defined for GBMs.[12] Nonetheless, further studies at longer times of implantation are required to discard systemic toxicity of the degradation products of these GBMs.

3. Conclusion

Based on the relevance of mechanical compliance and the softness of the spinal cord tissue, we herein focused on 3D soft aerogels for neural repair after SCI. In the absence of any additional biological functionalization or drug-loading, these foams mediated neural repair at the injured spinal cord by permitting excitatory myelinated axons to grow through the lesion site assisted by functional blood microvessels indicative of microvascular remodeling. These rGO foams clearly benefited the stabilization of the damage by avoiding scar retraction within the lesion site and decreasing perilesional areas of gliosis both above and below the SCI epicenter. Preliminary results by TEM evidenced, for the first time, ultrastructural changes compatible with ongoing degradative processes of the rGO sheets at the injured spinal cord. Finally, neither toxic responses in major organs nor changes in the spontaneous forelimb motor behaviour were induced by the chronic implantation of these rGO foams at 4 months. Future studies at longer time points will deepen on the *in vivo* degradation of rGO at the neural tissue, eventual systemic responses of toxicity derived and neuronal tracing for identifying the origin and destination of neurites populating the rGO foams.

4. Experimental Section

Material: GO slurry was purchased from Graphenea, S.A. (Batch #C1250/GOB125/D; 4,6 wt% concentration, > 95 % monolayer content). Neural cell culture media and supplements were acquired from Fisher Scientific. Chemical reagents were purchased from Sigma-Aldrich. Specific commercial details of antibodies are provided in Table S2. All reagents were used as received unless otherwise indicated.

Animals for scaffold implantation: Adult male Wistar rats were provided by the animal facilities of the *Hospital Nacional de Parapléjicos*. All the experimental protocols for surgical scaffold implantation at the spinal cord adhered to the regulations of the European Commission (directives 2010/63/EU and 86/609/EEC) and the Spanish government (RD53/2013 and ECC/566/2015) for the protection of animals used for scientific purposes.

Preparation of implantable rGO scaffolds: 3D rGO scaffolds were fabricated by a freeze-casting methodology. Briefly, GO slurry was gently dispersed in distilled water (5 wt%) and pipetted into tap covers of 0.5 ml Eppendorf tubes (50 μl). Samples were then frozen at -80 ℃ overnight and subsequently freeze-dried for 24 h. The resulting cylindrical and porous monoliths were thermally treated at 200 °C for 30 min. Prior to implantation, scaffolds were sterilized under UV radiation and spontaneously infiltrated with sterile tissue culture grade water at 4 ℃ for 48 h.

Physic-chemical characterization of GO slurry and rGO scaffolds: TEM studies were performed by using a Jeol JEM 1010 microscope (Tokyo, Japan) at 80-100 kV with a coupled digital camera (Gatan SC200, Pleasanton, CA, USA) for image acquisition. For SEM studies, a Hitachi S-3000N microscope working at 15kV with secondary electrons was used. XPS spectra were acquired at normal emission in an UHV chamber with a base pressure of 10^{-10} mbar equipped with a hemispherical electron energy analyzer (SPECS Phoibos 150 spectrometer) and a 2D delay-line detector, using a Mg Al-Kα (1253.6 eV) X-ray source. For experimental details on XPS studies, please refer to the Supplementary Material.

rGO scaffold implantation in hemisected rats: Adult male rats were used for scaffold implantation at the age of 20.0 ± 2.9 weeks (360.0 ± 35.8 g in weight). The amount of rGO implanted was 250 μg per animal (~700 μg kg^{-1}). The lesion model of choice was a

cervical unilateral hemisection at the right C6, rostral to the bulk of *triceps brachii* motoneurons. The rationale behind the selection of this model, in contrast to others such as contusions and complete transections, and specific technical details of the surgical procedures practiced have been discussed elsewhere.[36] In animals receiving rGO scaffolds, monoliths of appropriate dimensions were implanted at the lesion site to fill in the cavity created. Treatment groups included: control without injury (n = 6), injury (*I*, n = 9) and injury with implantation of rGO scaffold (*rGO*, n = 11). An exhaustive post-operatory care protocol was applied after surgery, with major attention placed into signs of pain, distress, dehydration, intestinal obstruction, and respiratory failure. After 4 months of implantation (120 DPI), animals were sacrificed by using a standard perfusion-fixation protocol and the thoraco-abdominal viscerae and spinal cords were extracted. All organs were examined macroscopically looking for any signs of gross damage before histological processing. In rats dedicated to TEM studies (control, n = 1; *I*, n = 3; *rGO*, n = 3), a specific perfusion-fixation procedure with a circulating solution containing paraformaldehyde at 4 % and glutaraldehyde at 1 % in phosphate buffer was conducted.

Behavioral tests: The degree of forelimb motor behavior compromise and its evolution over time was assessed by two different behavioral tests: grooming and forelimb asymmetry. Forelimb grooming function was assessed by using a scoring system. The forelimb asymmetry test allows detecting asymmetries in the paw use preference of the animal exploratory behavior caused by central nervous system injuries. For further experimental details and references on the behavior tests used, please refer to the Supplementary Material.

Atomic force microscopy and force spectroscopy: AFM measurements were performed by using a commercial instrument (JPK Nanowizard 3, JPK Instruments AG, Berlin,

Germany) mounted on a Axio Observer A1 inverted microscope (Carl Zeiss, Oberkochen, Germany). Depending on the biological sample (cells or tissues), different types of cantilevers were used. Force-distance curves were acquired to determine the Young's modulus of neural cells and spinal cord tissues. Embryonic neural progenitor cells for AFM testing of individual neural cells were gently provided by the *Hospital Nacional de Parapléjicos* (Toledo, Spain). For further experimental details on AFM studies, please refer to the Supplementary Material.

Magnetic resonance image (MRI) studies: The fragment between C4 and T1, which contains the main spinal cord structures involved in the rat anterior limb function, was prepared for MRI analysis. MRI images were acquired in a 7T Bruker Biospin MRI machine (Ettlingen, Germany) BioSpec 70/30. The different measurements were made using images of a turbo spin echo sequence enhanced in T2 (RARE turbo) and axial acquisition. For further experimental details on MRI studies, please refer to Supplementary Material.

Histological studies: All perfused tissue samples were placed in paraformaldehyde 4 % at 4 °C overnight and then 3 days in sucrose (30 % in phosphate buffer saline, PBS) at 4 °C for cryo-protection. Tissue pieces were mounted on plastic containers, quick-frozen in Optimal Cutting Temperature compound (Tissue Tek, Hatfield, PA) and cut in horizontal sections of 10-µm by using a Leica CM1900 cryostat with an angle of 10º. In the particular case of spinal cords, the entire C5-C7 fragment was cut in sagittal sections from right to left. Organs were stained with conventional hematoxylin-eosin (HE) stain. Spinal cords were examined after Masson's trichrome for visualizing collagen. In all cases, panoramic images at low magnification were collected by using an Olympus BX61 microscope.

TEM studies of rGO implants and organs: Samples dedicated to TEM studies were additionally post-fixed in osmic tetroxide (1% in distilled water) for 1 h. Dehydration was then followed by immersion in successive solutions of ethanol at increasing concentrations (30, 50, 70, 95, and 100 %), with a final step in pure acetone. Samples were then included in *Durcupán* resin by consecutive steps at increasing concentrations (1:3, 1:1, 3:1 in acetone). Final samples in pure resin were polymerized at 60 ºC for 48 h. Ultrathin sections (*ca.* 60 nm) were obtained and subsequently stained with uracil acetate and lead citrate. The visualization was carried out by using a Jeol JEM 1010 microscope at 80-100 kV. Images were processed by using the *Fiji* software for quantitative estimations. Features of rGO degradation were estimated by analyzing the distribution of pixels in the grey scale from images captured at 300,000X at 100 kV in similar conditions of brightness (N ≥ 25 from 3 different animals per group). Cavities at the lesion site and tissue infiltration degree were estimated by studying the distribution of pixels in the grey scale from images captured at 2,000X at 80 kV in similar conditions (N ≥ 20 from 3 different animals per group).

Immunofluorescence studies: Specific details for each of the antibodies used in this study are summarized in **Table S2**. Spinal cord samples were examined for the presence of the following markers: (1) map-2 for somas and dendrites in neurons, (2) tau for axons in neurons, (3) vimentin for non-neuron cells including glial and connective tissue cells, (4) glial fibrillary acidic protein (GFAP) for astrocytes, (5) ED1 for macrophages, (6) platelet-derived growth factor receptor β (PDGFRβ) for pericytes, precursors of oligodendrocytes and connective tissue cells such as fibroblasts, (7) SMI-311 for cytoskeletal neurofilaments in neurites, (8) β-III tubulin for cytoskeleton microtubules in neurites, (9) RECA-1 for endothelial cells in blood vessels, (10) laminin for basement membranes in blood vessels, (11) vesicular glutamate transporter 2

(Vglut2) for excitatory glutamatergic fibers, (12) tyrosine hydroxylase for excitatory dopaminergic fibers, and (13) serotonin for inhibitory serotoninergic fibers. Appropriate secondary antibodies were selected accordingly. In all cases, cell nuclei were visualized by labeling with Hoechst (1 mg mL^{-1}). Fluorescence images were collected by using a Leica TCS SP5 microscope. Capture conditions were fixed by using sections from the three experimental groups incubated with the secondary antibodies but without the primary ones. All images were thereafter captured under these conditions. All fluorescence images were automatically quantified by using a customized macro in *Fiji* software as the number of pixels (correspondent μm^2) positively stained for each particular fluorescence marker after the definition of the correspondent threshold of positive labeling. Control spinal cords and contralateral hemicords in injured animals served as reference values to define correspondent threshold values for each marker. At least three non-overlapping images at 40X per animal were acquired in each position of interest (N $\geq$ 9 per fluorescence marker, study region and group from at least 3 different animals per group). Areas under study were: left hemicord – LH-, perilesional areas at 1-2 mm from the lesion site – PL12-, caudal interface of the lesion – CIF-, rostral interface of the lesion – RIF-, lesion site without scaffold, and lesion site with scaffold. Additional bright field images were taken to define scaffold location.

Statistics: Values were expressed as mean ± standard deviation of at least three different animals per group (N $\geq$ 3). In the box plots, the line and square inside correspond to the median and the mean of the distribution, respectively. The top and bottom of the box represent, respectively, the 75th and 25th percentiles. The whiskers out of the box denote the range of outer-most data that fall within 1.5 x interquartile range. Additionally, single data points were overlapped with their correspondent box plots. Statistical analysis was performed by using the Statistical Package for the Social

Sciences (SPSS, version 17.0), except for AFM measurements that were analyzed by using the Origin platform (OriginLab). Comparisons among groups were done by one-way analysis of variance (ANOVA) and either *post-hoc Scheffé* or *Games-Howell* tests (homogeneous *vs.* heterogeneous variances, respectively, as dictated by Levene's test). For comparisons between two independent groups, a *T-test* was used. MRI data were compared by using the Mann Whitney Rank sum test. In all cases, the significance level was defined as $p < 0.05$.

Supporting Information
Supporting Information is available from the Wiley Online Library or from the author.

Received: ((will be filled in by the editorial staff))
Revised: ((will be filled in by the editorial staff))
Published online: ((will be filled in by the editorial staff))

References

[1] S. Y. Park, J. Park, S. H. Sim, M. G. Sung, K. S. Kim, B. H. Hong, S. Hong, *Adv. Mater.* **2011**, *23*, H263.

[2] S. Marchesan, L. Ballerini, M. Prato, *Science* **2017**, *356*, 1010.

[3] Y. Wang, W. C. Lee, K. K. Manga, P. K. Ang, J. Lu, Y. P. Liu, C. T. Lim, K. P. Loh, *Adv. Mater.* **2012**, *24*, 4285.

[4] N. Li, X. Zhang, Q. Song, R. Su, Q. Zhang, T. Kong, L. Liu, G. Jin, M. Tang, G. Cheng, *Biomaterials* **2011**, *32*, 9374.

[5] M. Tang, Q. Song, N. Li, Z. Jiang, R. Huang, G. Cheng, *Biomaterials* **2013**, *34*, 6402.

[6] R. Rauti, N. Lozano, V. León, D. Scaini, M. Musto, I. Rago, F. P. Ulloa Severino, A. Fabbro, L. Casalis, E. Vázquez, K. Kostarelos, M. Prato, L. Ballerini, *ACS Nano* **2016**, *10*, 4459.

[7] N. P. Pampaloni, M. Lottner, M. Giugliano, A. Matruglio, F. D'Amico, M. Prato, J. A. Garrido, L. Ballerini, D. Scaini, *Nat. Nanotechnol.* **2018**. DOI:.10.1038/s41565-018-0163-6.

[8] Y. Qian, X. Zhao, Q. Han, W. Chen, H. Li, W. Yuan, *Nat. Commun.* **2018**, *9*, 323.

[9] C. Defterali, R. Verdejo, L. Peponi, E. D. Martín, R. Martínez-Murillo, M. Á. López-Manchado, C. Vicario-Abejón, *Biomaterials* **2015**, *82*, 84.

[10] K. E. Kitko, T. Hong, R. M. Lazarenko, D. Ying, Y. Q. Xu, Q. Zhang, *Nat. Commun.* **2018**, *9*, 796.

[11] A. Bianco, *Angew. Chem. Int. Ed.* **2013**, *52*, 4986.

[12] G. Reina, J. M. González-Domínguez, A. Criado, E. Vázquez, A. Bianco, M. Prato, *Chem. Soc. Rev.* **2017**, *46*, 4400.

[13] Y. Li, L. Feng, X. Shi, X. Wang, Y. Yang, K. Yang, T. Liu, G. Yang, Z. Liu, *Small* **2014**, *10*, 1544.

[14] R. Kurapati, S. P. Mukherjee, C. Martín, G. Bepete, E. Vázquez, A. Pénicaud, B. Fadeel, A. Bianco, *Angew. Chem. Int. Ed. Engl.* **2018**. DOI:.10.1002/anie.201806906.

[15] R. Kurapati, J. Russier, M. A. Squillaci, E. Treossi, C. Ménard-Moyon, A. E. Del Río-Castillo, E. Vazquez, P. Samorí, V. Palermo, A. Bianco, *Small* **2015**, *11*, 3985.

[16] D. Guarnieri, P. Sánchez-Moreno, A. E. Del Rio Castillo, F. Bonaccorso, F. Gatto, G. Bardi, C. Martín, E. Vázquex, T. Catelani, S. Sabella, P. P. Pompa, *Small* **2018**. DOI: 10.1002/smll.201800227.

[17] C. Göritz, D. O. Dias, N. Tomilin, M. Barbacid, O. Shupliakov, J. Frisén, *Science* **2011**, *333*, 238.

[18] E. Moeendarbary, I. P. Weber, G. K. Sheridan, D. E. Koser, S. Soleman, B. Haenzi, E. J. Bradbury, J. Fawcett, K. Franze, *Nat. Commun.* **2017**, *8*, 14787.

[19] M. M. Pathak, et al., *Proc. Natl. Acad. Sci. U.S.A.* **2014**, *111*, 16148.

[20] D. Koch, W. J. Rosoff, J. Jiang, H. M. Geller, J. S. Urbach, *Biophys. J.* **2012**, *102*, 452.

[21] P. Moshayedi, F. Costa Lda, A. Christ, S. P. Lacour, J. Fawcett, J. Guck, K. Franze, *J. Phys. Condens. Matter.* **2010**, *22*, 194114.

[22] National Spinal Cord Injury Statistical Center, Facts and Figures at a Glance. Birmingham, AL: University of Alabama at Birmingham, **2015**. https://www.nscisc.uab.edu/Public/Facts%20and%20Figures%20-%202018.pdf. Last retrieved: 07/31/2018.

[23] A. de los Reyes-Guzmán, E. López-Dolado, V. Lozano-Berrio, S. Pérez-Nombela, D. Torricelli, J. L. Pons, A. Gil-Agudo, *JSM Physical. Med. Rehabil.* **2017**, *1*, 1004.

[24] J. E. Collazos-Castro, V. M. Soto, M. Gutiérrez-Davila, M. Nieto-Sampedro, *J. Neurotrauma* **2005**, *22*, 544.

[25] J. F. Ditunno, *Spinal Cord* **2004**, *42*, 383.

[26] I. R. Minev, P. Musienko, A. Hirsch, Q. Barraud, N. Wenger, E. M. Moraud, J. Gandar, M. Capogrosso, T. Milekovic, L. Asboth, R. F. Torres, N. Vachicouras, Q. Liu, N. Pavlova, S. Duis, A. Larmagnac, J. Vörös, S. Micera, Z. Suo, G. Courtine, S.P. Lacour, *Science* **2015**, *347*, 159.

[27] R. Van der Brand, J. Heutschi, Q. Barraud, J. DiGiovanna, K. Bartholdi, M. Huerlimann, L. Friedli, I. Vollenweider, E. M. Moraud, S. Duis, N. Dominici, S. Micera, P. Musienko, G. Courtine, *Science* **2012**, *336*, 1182.

[28] T. Führmann, M. S. Shoichet, *Biomed. Mater.* **2018**, *13*, 050201.

[29] T. Führmann, P. N. Anandakumaran, M. S. Shoichet, *Adv. Healthc. Mater.* **2017**, *6*. DOI: 10.1002/adhm.201601130.

[30] A. E. Haggerty, I. Maldonado-Lasunción, M. Oudega, *Biomed. Mater.* **2018**, *13*, 044105.

[31] J. R. Slotkin, C. D. Pritchard, B. Luque, J. Ye, R. T. Layer, M. S. Lawrence, T. M. O'Shea, R. R. Roy, H. Zhong, I. Vollenweider, V. R. Edgerton, G. Courtine, E. J. Woodard, R. Langer, *Biomaterials* **2017**, *123*, 63.

[32] L. T. A. Hong, Y. M. Kim, H. H. Park, D. H. Hwang, Y. Cui, E. M. Lee, S. Yahn, J. K. Lee, S. C. Song, B. G. Kim, *Nat. Commun.* **2017**, *8*, 533.

[33] J. S. Rao, C. Zhao, A. Zhang, H. Duan, P. Hao, R. H. Wei, J. Shang, W. Zhao, Z. Liu, J. Yu, K. S. Fan, Z. Tian, Q. He, W. Song, Z. Yang, Y. E. Sun, X. Li, *Proc. Nat. Acad. Sci. U.S.A.* **2018**, *115*, E5595.

[34] S. Usmani, E. R. Aurand, M. Medelin, A. Fabbro, D. Scaini, J. Laishram, F. B. Rosselli, A. Ansuini, D. Zoccolan, M. Scarselli, M. De Crescenzi. S. Bosi, M. Prato, L. Ballerini, *Sci. Adv.* **2016**, *2*, e1600087.

[35] A. Fabbro, A. Villari, J. Laishram, D. Scaini, F. M. Toma, A. Turco, M. Prato, L. Ballerini, *ACS Nano* **2012**, *6*, 2041.

[36] E. López-Dolado, A. González-Mayorga, M. T. Portolés, M. J. Feito, M. L. Ferrer, F. Del Monte, M. C. Gutiérrez, M. C. Serrano, *Adv. Healthc. Mater.* **2015**, *4*, 1861.

[37] E. López-Dolado, A. González-Mayorga, M. C. Gutiérrez, M. C. Serrano, *Biomaterials* **2016**, *99*, 72.

[38] Y. B. Lu, K. France, G. Seifert, C. Steinhäuser, F. Kirchhoff, H. Wolburg, J. Guck, P. Janmey, E-Q. Wei, J. Käs, A. Reichenbach, *Proc. Natl. Acad. Sci. U.S.A.* **2006**, *103*, 17759.

[39] F. Della Pellea, R. Di Battistaa, L. Vázquez, F. J. Palomares, M. Del Carlo, M. Sergi, D. Compagnone, A. Escarpa, *Appl. Mater. Today* **2017**, *9*, 29.

[40] P. D. Garcia, R. Garcia, *Biophys. J.* **2018**, *114*, 2923.

[41] P. D. Garcia, C. R. Guerrero, R. Garcia, *Nanoscale* **2017**, *9*, 12051.

[42] J. Kiernan, *Micros. Today* **2000**, *12*, 8.

[43] S. Kubinová, D. Horák, A. Hejcl, Z. Plichta, J. Kotek, V. Proks, S. Forostyak, E. Syková . *J. Tissue Eng. Regen. Med.* **2015**, *9*, 1298.

[44] S. Kubinová, D. Horák, A. Hejčl, Z. Plichta, J. Kotek, E. Syková, *J. Biomed. Mater. Res. Part A* **2011**, *99*, 618.

[45] E. C. Tsai, P. D. Dalton, M. S. Shoichet, C. H. Tator, *Biomaterials* **2006**, *27*, 519.

[46] D. Shahriari, J. Y. Koffler, M. H. Tuszynski, W. M. Campana, J. S. Sakamoto, *Tissue Eng. Part A* **2017**, *23*, 415.

[47] N. A. Silva, A. J. Salgado, R. A. Sousa, J. T. Oliveira, A. J. Pedro, H. Leite-Almeida, R. Cerqueira, A. Almeida, F. Mastronardi, J. F. Mano, N. M. Neves, N. Sousa, R. L. Reis, *Tissue Eng. Part A* **2010**, *16*, 45.

[48] J. E. McKenna, G. T. Prusky, I. Q. Whishaw, *J. Comp. Neurol.* **2000**, *419*, 286.

[49] E. López-Dolado, A. Lucas-Osma, J. E. Collazos-Castro, *J. Neurotrauma* **2013**, *30*, 191.

[50] M. Itzkovich, H. Shefler, L. Front, R. Gur-Pollack, K. Elkayam, V. Bluvshtein, I. Gelernter, A. Catz, *Spinal Cord* **2018**, *56*, 46.

[51] L. Filli, B. Zörner, O. Weinmann, M. E. Schwab, *Brain* **2011**, *134*, 2261.

[52] A. de los Reyes-Guzmán, A. Gil-Agudo, B. Peñasco-Martín, M Solís-Mozos, A. del Ama-Espinosa, E. Pérez-Rico, *J. Neuroeng. Rehabil*. **2010**, *7*, 41.

[53] J. W. Austin, M. Afshar, M. G. Fehlings, *J Neurotrauma* **2012**, *29*, 1838.

[54] Y. Karam, P. W. Hitchon, N. E. Mhanna, W. He, J. Noeller, *Clin. Neurol. Neurosurg.* **2014**, *124*, 44.

[55] J. T. Yabe, W. K. Chan, F. S. Wang, A. Pimenta, D. D. Ortiz, T. B. Shea, *Cell Motil. Cytoskeleton* **2003**, *56*, 193.

[56] S. A. Moody, M. S. Quigg, A. Frankfurter, *J. Comp. Neurol.* **1989**, *279*, 567.

[57] M. K. Lee, J. B. Tuttle, L. I. Rebhun, D. W. Cleveland, A. Frankfurter, *Cell Motil. Cytoskeleton* **1990**, *17*, 118.

[58] D. Panda, H. P. Miller, A. Banerjee, R. F. Luduena, L. Wilson, *Proc. Natl. Acad. Sci. U.S.A.* **1994**, *91*, 11358.

[59] L. Filli, A. K. Engmann, B. Zörner, O. Weinmann, T. Moraitis, M. Gullo, H. Kasper, R. Schneider, M. E. Schwab, *J. Neurosci.* **2014**, *34*, 13399.

[60] M. Ballerman, K. Fouad, *Eur. J. Neurosci.* **2006**, *23*, 1988.

[61] J. R. Flynn, B. A. Graham, M. P. Galea, R. J. Callister, *Neuropharmacology* **2011**, *60*, 809.

[62] G. Courtine, B. Song, R. R. Roy, H. Zhong, J. E. Herrmann, Y. Ao, J. Qi, V. R. Edgerton, M. V. Sofroniew, *Nat. Med.* **2008**, *14*, 69.

[63] N. Nishimura, Y. Morichika, T. Isa, *Brain* **2009**, *132*, 709.

[64] M. S. Esposito, P. Capelli, S. Arber, *Nature* **2014**, *508*, 351.

[65] M. Hägglund, L. Borgius, K. J. Dougherty, O. Kiehn, *Nat. Neurosci.* **2010**, *13*, 246.

[66] E. R. Burnside, E. J. Bradbury, *Neuropathol. Appl. Neurobiol.* **2014**, *40*, 26.

[67] L. R. Nih, S. Gojgini, S. T. Carmichael, T. Segura, *Nat. Mater.* **2018**. DOI: .

[68] A. Campana, T. Cramer, D. T. Simon, M. Berggren, F. Biscarini, *Adv. Mater.* **2014**, *26*, 3874.

[69] H. Yue, W. Wei, Z. Yue, B. Wang, N. Luo, Y. Gao, D. Ma, G. Ma, Z. Su, *Biomaterials* **2012**, *33*, 4013.

[70] Q. Mu, G. Su, L. Li, B. O. Gilbertson, L. H. Yu, Q. Zhang, Y. P. Sun, B. Yan, *ACS Appl. Mater. Interfaces* **2012**, *4*, 2259.

[71] K. Wang, J. Ruan, H. Song, J. Zhang, Y. Wo, S. Guo, D. Cui, *Nanoscale Res. Lett.* **2011**, *6*, 1.

[72] X. Zhang, J.Yin, C. Peng, W. Hu, Z. Zhu, W. Li, C. Fan, Q. Huang, *Carbon* **2011**, *49*, 986.

[73] J. H. Liu, S. T. Yang, H. Wang, Y. Chang, A. Cao, Y. Liu, *Nanomedicine (Lond)* **2012**, *7*, 1801.
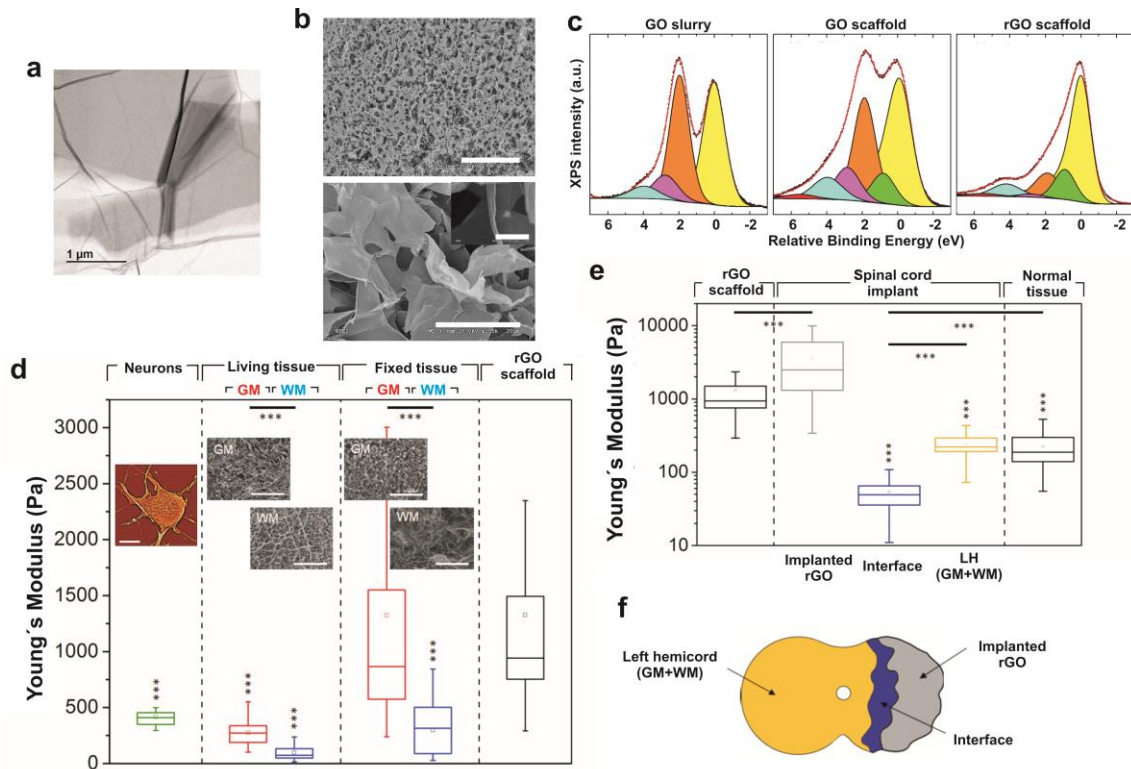
Figure 1. Physic-chemical characterization of rGO foams. (a) Representative TEM image of GO sheets. (b) Morphological characterization of the 3D rGO foams by SEM. Scale bars: 500 μm (top), 20 μm (bottom) and 5 μm (inset). (c) XPS spectra of the C1s corresponding to the GO slurry, GO scaffold and rGO scaffold together with fit composed of chemically shifted components associated to different C chemical bonding, respectively. XPS spectra were normalized to maximum intensity peak in each case. Data points are represented as black symbols and Shirley background and component peaks using solid lines. The fitting curve (red line) resulted from the addition of contributions belonging to: C=C graphitic structures (yellow), C-H or C-C defective graphitic, sp3 configurations (green), C-OH carbonyl groups (orange), O-C-O carbonyl groups (magenta), O-C=O carboxylic groups (cyan), and π-π* transitions coming from graphitic structures (red). (d) Nanomechanical characterization of spinal cord tissue (GM and WM), neural cells and rGO scaffolds as obtained from AFM-based measurements (expressed as Young's moduli). Topographical image of the cytoskeleton of a neuron as measured by AFM (scale bar: 10 μm). SEM images of living and fixed spinal cords at both GM and WM (scale bars: 100 μm). GM: grey matter; WM: white matter. (e) Nanomechanical characterization of 4-months rGO implants and spinal cord tissue. Statistics: p < 0.001***. Horizontal asterisks indicate comparisons as indicated; vertical asterisks refer to comparisons with rGO scaffold. (f) Scheme of the main regions under study on the rGO-implanted spinal cord tissue.
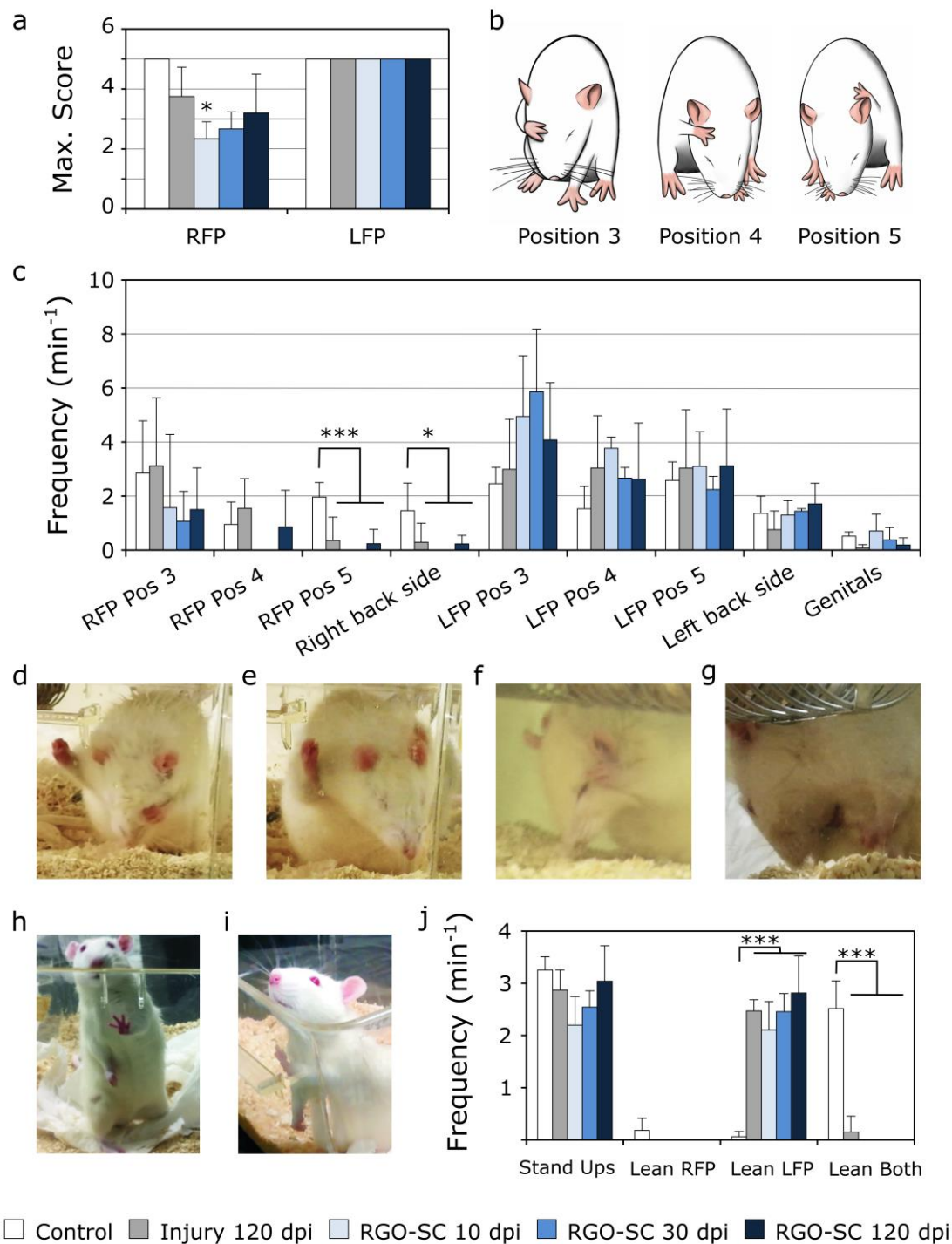
Figure 2. Behavioral tests on rGO rats as measured by grooming (a-g) and asymmetry (h-j) tests. (a) Maximum score numbers achieved for the RFP and LFP during grooming. (b) Scheme of the relevant grooming positions. (c) Frequency of the different positions reached during grooming for the RFP and LFP. (d,e) Representative photographs of rGO rats failing positions 4 and 5 with the RFP, respectively. (f,g) Representative photographs of rGO rats attaining position 5 with the RFP and grooming on the right back side, respectively. (h,i) Frontal and lateral views of a representative rGO rat leaning on the cage wall, respectively. (j) Frequency of stand-ups and supports on RFP, LFP and both forepaws during asymmetry tests. Statistics: $p < 0.05$* and $p < 0.005$***. LFP: left forepaw; RFP: right forepaw.
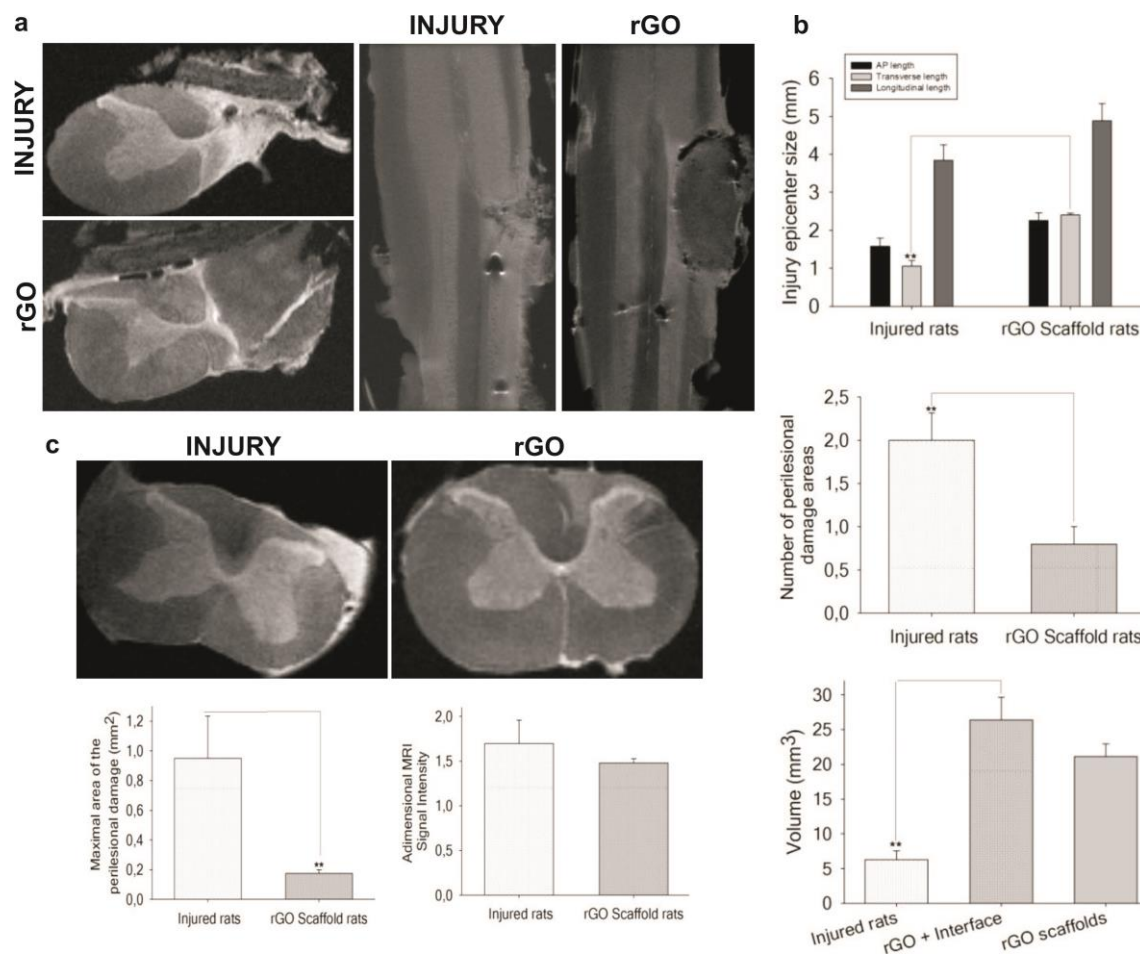
Figure 3. MRI and histological features of the rGO implants. (a) Representative spinal cord MRI images corresponding to: axial scans (left column) and coronal scans (right column) of *I* and *rGO* rats. (b) Quantifications of de lesion epicenter size and volume and the number of perilesional damage areas. (c) Axial scans of representative perilesional damaged areas in *I* and *rGO* rats and respectivequantifications.
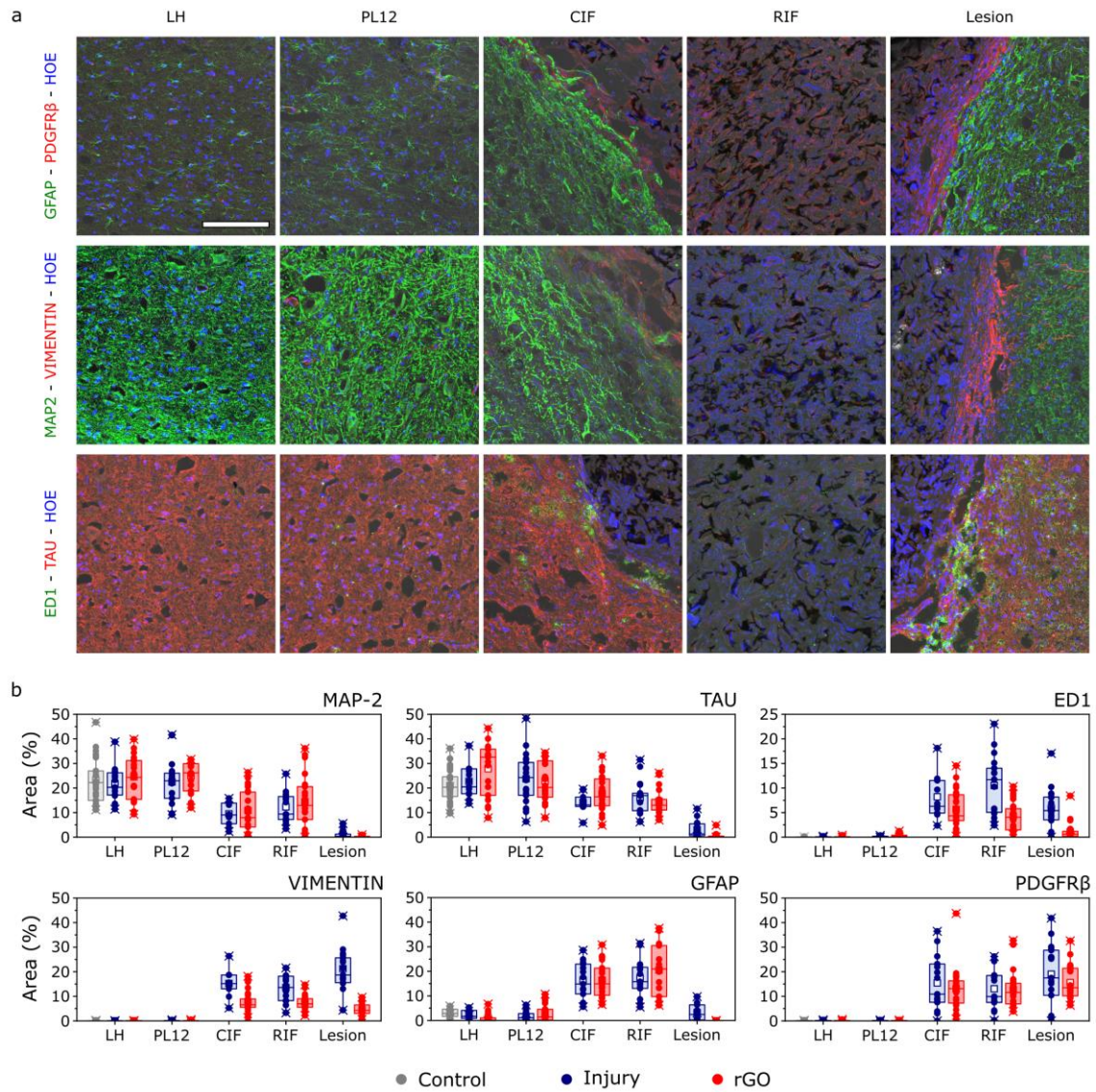
Figure 4. Immunofluorescence characterization of the lesion site in rGO rats. (a) Representative CLSM images for the different markers and areas under study. Scale bar: 150 μm. (b) Quantitative data from immunofluorescence images. CIF: caudal interface; LH: left hemicord; PL12: perilesional areas at 1-2 mm from the lesion border; RIF: rostral interface.
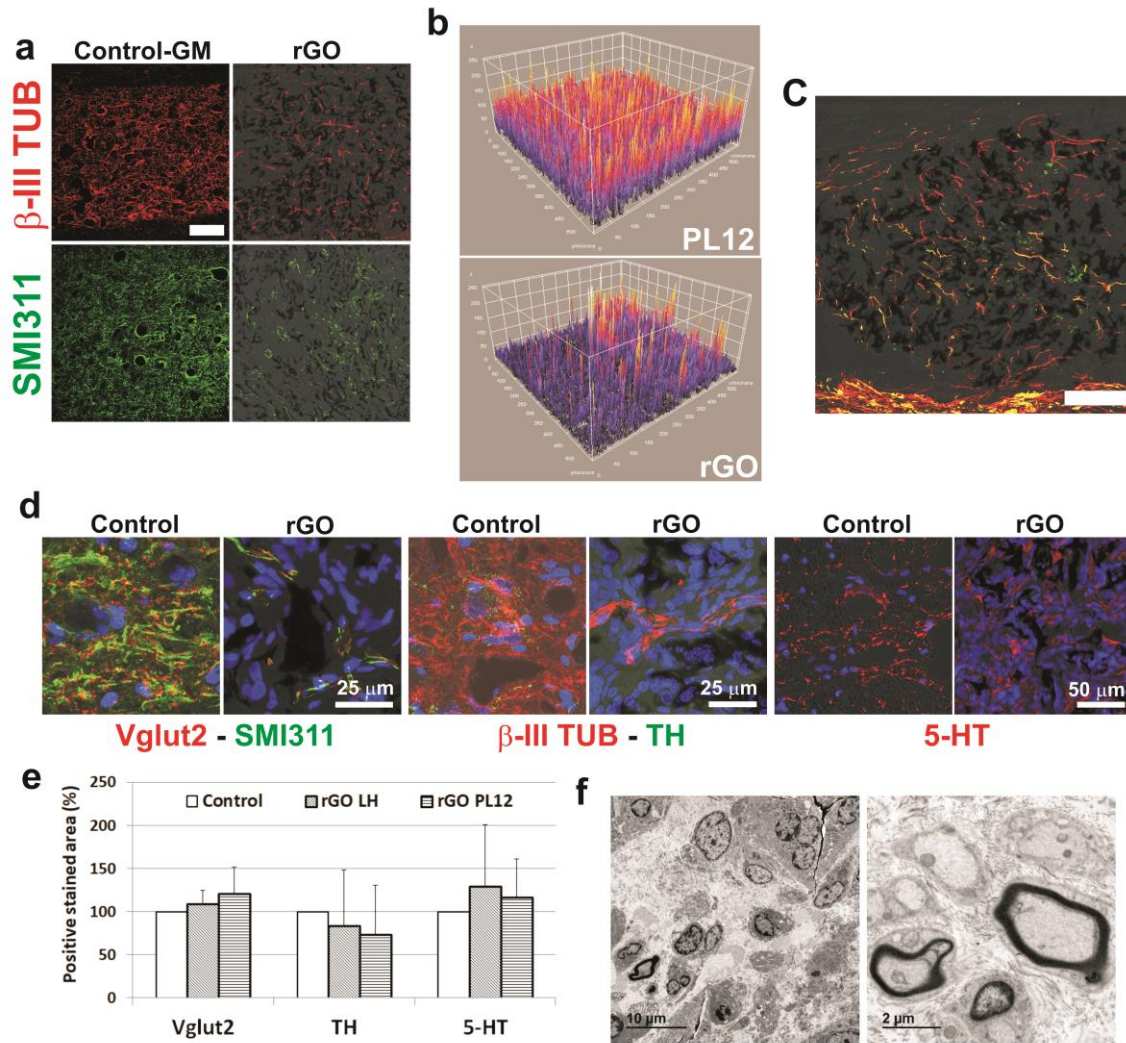
Figure 5. Axon growth at the lesion site in rGO rats. (a) Representative CLSM images for β-III tubulin and SMI311. GM in control rats is shown for comparison. Scale bars: 150 μm. (b) 3D reconstruction plots for β-III tubulin in PL12 and rGO (image area 555.61 μm x 555.61 μm). (c) Illustrative CLSM image merging β-III tubulin and SMI311 labeling. Scale bar: 150 μm. (d) Representative CLSM images for Vglut2, TH and 5-HT in control and rGO rats. Counterstaining with SMI311 and β-III tubulin for neurites location. Cell nuclei stained with Hoechst. (e) Quantitative data for Vglut2, TH and 5-HT at LH and PL12 in comparison to GM in control rats. (f) Representative TEM images evidencing the presence of myelinated axons within rGO scaffolds. GM: grey matter; LH: left hemicord; PL12: perilesional areas at 1-2 mm from the lesion border; TH: tyrosine hydroxylase; Vglut2: vesicular glutamate transporter 2; 5-HT: serotonin.
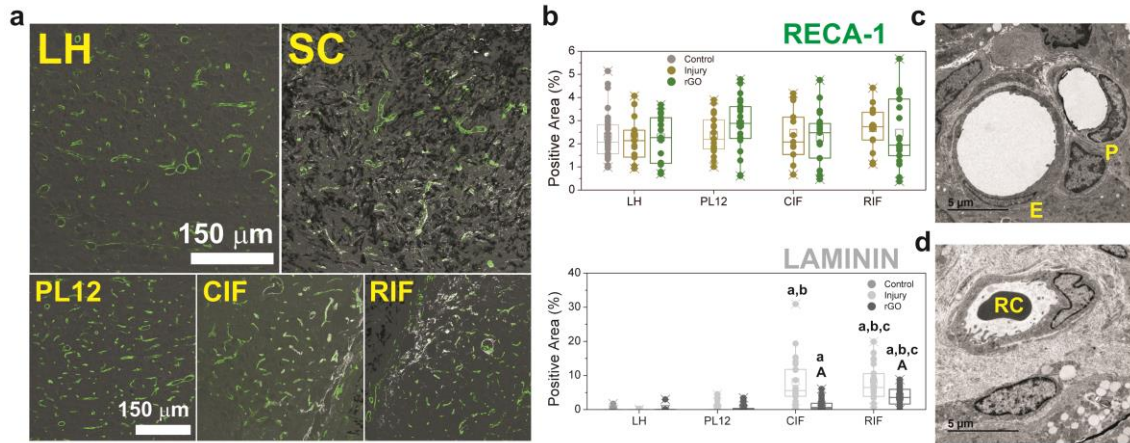
Figure 6. Analysis of microvessels formation in rGO rats. (a) Representative immunofluorescence images for Reca-1 and laminin at the different areas under study. (b) Quantitative data from immunofluorescence images for both markers. Values for control and injured rats without scaffolds are shown for comparison. CIF: caudal interface; LH: left hemicord; PL12: perilesional areas at 1-2 mm from the lesion border; RIF: rostral interface. Statistics: significant differences with respect to (a) LH, (b) PL12, (c) CIF, and (A) *I* group ($p < 0.05$). Representative TEM images illustrating (c) the wall structure of the microvessels formed containing mature endothelial cells (E) and pericytes (P) and (d) their functional nature demonstrated by the presence of red blood cells (RC).
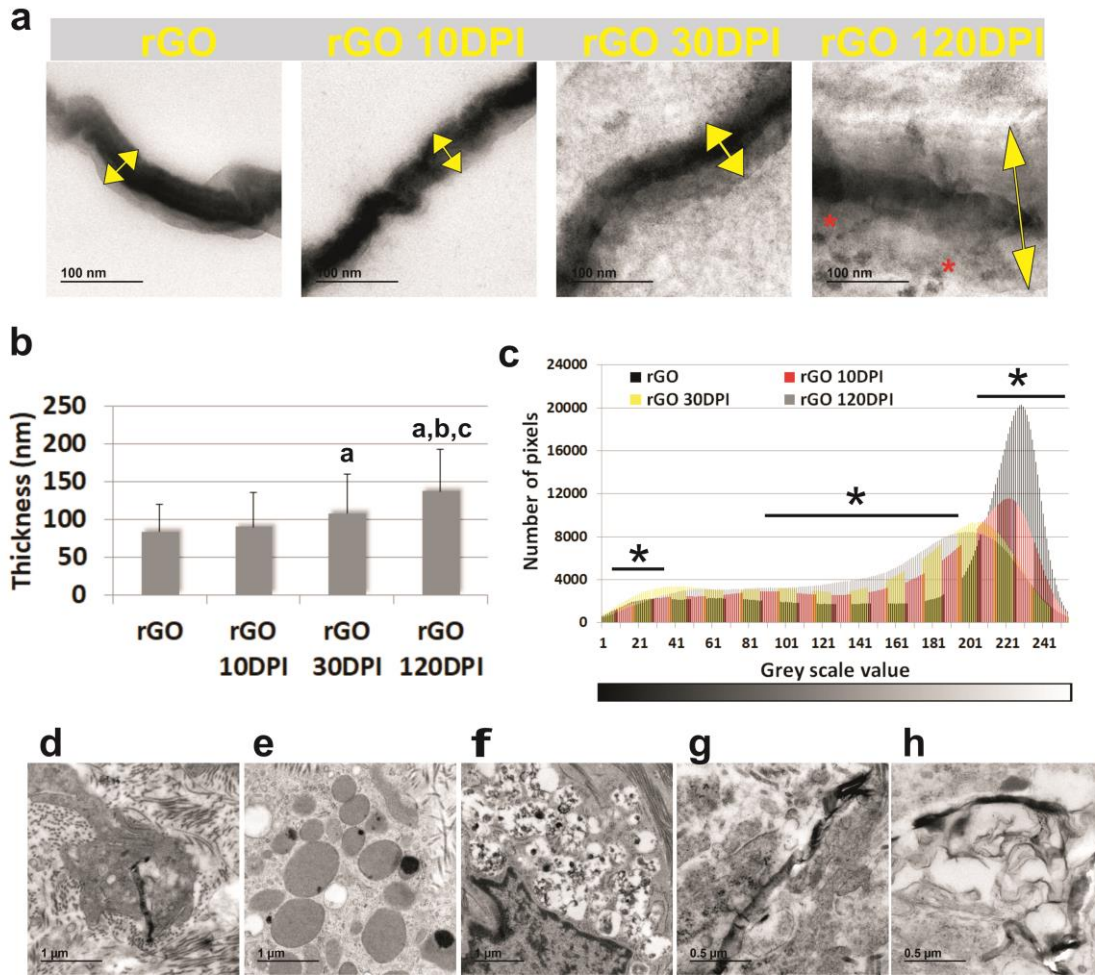
Figure 7. Degradation features in rGO rats. (a) Representative high-magnification TEM images illustrating details of rGO foams over implantation time. Yellow arrows indicate rGO scaffold wall thickness and red asterisks point out degradation clues in their immediate periphery. (b) Wall thickness variation over time. Statistics: significant differences with respect to (a) rGO, (b) rGO 10DPI, and (c) rGO 30DPI ($p < 0.05$). (c) Pseudo-quantitative estimations of rGO scaffold degradation by analyses of the variations in grey-scale pixels of TEM images. Statistics: $p < 0.05$*. (d-h) Specific rGO degradation features from high magnification TEM images.

3D porous rGO foams chronically implanted in the injured spinal cord transmit mechanically compliant signals to the neural tissue and support microvascular remodeling and excitatory neurites growth throughout the lesion site. No mechanical distress is induced in the surrounding spinal cord tissue while diminishing perilesional damage. Initial features of rGO degradation without systemic toxic effects are identified.

Ana Domínguez-Bajo, Ankor González-Mayorga, Carlos R. Guerrero, F. Javier Palomares, Ricardo García, Elisa López-Dolado, and María Concepción Serrano*

Myelinated axons and functional blood vessels populate mechanically compliant rGO foams in chronic cervical spinal cord hemisected rats
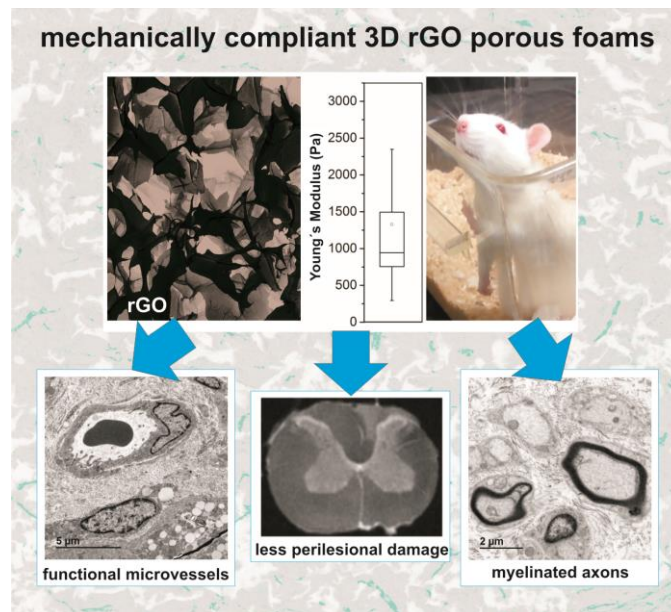
Supporting Information

Myelinated axons and functional blood vessels populate mechanically compliant rGO foams in chronic cervical spinal cord hemisected rats

Ana Domínguez-Bajo,[1] Ankor González-Mayorga,[2] Carlos R. Guerrero-Rodríguez,[1] F. Javier Palomares,[1] Ricardo García,[1] Elisa López-Dolado,[2,3] and María Concepción Serrano[1,]*

Extended Experimental Section

Physic-chemical characterization of GO slurry and rGO scaffolds: TEM studies were performed by using a Jeol JEM 1010 microscope (Tokyo, Japan) at 80-100 kV with a coupled digital camera (Gatan SC200, Pleasanton, CA, USA) for image acquisition. For SEM studies, a Hitachi S-3000N microscope working at 15kV with secondary electrons was used. XPS spectra were acquired at normal emission in an UHV chamber with a base pressure of 10^{-10} mbar equipped with a hemispherical electron energy analyzer (SPECS Phoibos 150 spectrometer) and a 2D delay-line detector, using a Mg Al-Kα (1253.6 eV) X-ray source. The spectra were analyzed with the CasaXPS program using a Shirley method for background subtraction, for X-ray source satellite removal, and data processing for quantitative XPS analysis. The absolute binding energies of the photoelectron spectra were determined by referencing to the sp^2 transition of C1s at 284.6 eV determined from a freshly cleaved HOPG (Highly Oriented Pyrolytic Graphite) sample. The overall sample composition was determined from survey spectrum taken at a pass energy of 20eV. It showed intense C1s and O1s peaks as well as a minor contribution from Na1s, Mn2p and K2p (only in GO-slurry sample), and S2p. C/O atomic concentrations were determined by measuring C1s and O1s spectra with a pass

energy and energy step of 20 and 0.10 eV, respectively, which provided the elemental content of C and O as seen in **Table S1**. For a detailed analysis, C1s high-resolution core level spectra were recorded using an energy step of 0.025 eV and a pass-energy of 10 eV to obtain the narrowest lineshape analysis and proper core level fitting. XPS spectra fitting was done by using the deconvolution of an asymmetric component characteristic of C sp2 bonding and several mixed percentage of Gaussian-Lorentzian symmetric functions for the rest of components, keeping the fwhm and the Gaussian/Lorentzian ratio constant. The energy of the peaks and their relative heights were determined by a least-squares method to account for the emission ascribed to the different chemical environment of carbon atoms according to the values reported.[1]

Behavioral tests: The degree of forelimb motor behavior compromise and its evolution over time were assessed by two different behavioral tests: grooming and forelimb asymmetry. Forelimb grooming function was assessed by using a scoring system adapted from previously described protocols.[2,3] Briefly, tap water was applied to the animal's head and cervical back area with a soft gauze. Stereotypical grooming sequences of at least 50 s of duration were recorded for each animal in their own cage with a video camera. Forelimb scoring was defined as follows: (1) licking of the forepaws and mouth/nose washing, (2) grooming of the area between the nose and the eyes without reaching eyes, (3) grooming of the area between the eyes and the ears without reaching ears, (4) grooming of the ears area, and (5) grooming of the back area behind the ears. Grooming of the back left and right sides and genitals area were also scored. Slow motion video playback (speed = 0.20x) was used to score each forelimb independently. Values were expressed as a function of time.

The forelimb asymmetry test allows detecting asymmetries in the paw use preference of the animal exploratory behavior caused by central nervous system

injuries.[4,5] In order to minimize stress, the spontaneous exploratory behavior was recorded for over 5 min in their own cage. When animals were found dramatically inactive, stimuli such as water, paper, food pellets, and tricks (cereal flakes) were used to get them back to an active exploratory behavior. Videos with more than 60 s of animal inactivity were discarded and recorded periods of inactivity longer than 30 s excluded from analyses. Selected variables of study were: (i) the number of stand-ups on hindlimbs (*StaUp*) and the number of times that the animal leant on the cage walls by using their (ii) right forepaw (*LeanRFP*), (iii) left forepaw (*LeanLFP*) or (iv) both (*LeanBoth*). Additional attention was placed on the morphology of the paw contact (either open –palm– or close –fist–). Finally, the capacity of the animal to change leaning points with the forepaws while standing up was also observed.

Atomic force microscopy and force spectroscopy: AFM measurements were performed by using a commercial instrument (JPK Nanowizard 3, JPK Instruments AG, Berlin, Germany) mounted on a Axio Observer A1 inverted microscope (Carl Zeiss, Oberkochen, Germany). Depending on the biological sample (cells or tissues), different types of cantilevers were used. For spinal cord slices, we used a modified tipless silicon cantilever (Arrow-TL1, NanoWorld, Neuchtel, Switzerland) with a nominal spring constant of 0.07 N m^{-1} and a resonant frequency of 6 kHz. We glued a polystyrene bead with 50 μm of diameter (microParticles GmbH, Germany) to the free end of the cantilever (Norland Optical Adhesive 63, Norland Products Inc., Cranbury, NJ, USA). For cells, we used cantilevers characterized by a spring constant of 0.08 N m^{-1}, a resonant frequency of 17 kHz and a spherical tip with 6.62 μm of diameter (CP-PNPL-SiO-C cantilevers sQube, Bickenbach, Germany). The cantilever spring constant k was determined by using the thermal noise method as implemented in the AFM software (JPK Nanowizard 3).

Force-distance curves were acquired to determine the Young's modulus of neural cells and spinal cord tissues. The tip-sample distance was modulated by applying a triangular waveform. For the tissues, the modulation velocity was 5 μm s^{-1} (modulation frequency of 0.33 Hz) and the maximum force applied was 20 nN (Figure S2). Data represents the average value obtained in three different spinal cord slices. In each sample, 100 individual force-distance curves were taken. The individual force-distance curves were acquired on different locations separated by approximately 100 μm. For the neural cells, the tip velocity was 5 μm s^{-1} (modulation frequency of 1Hz) and the maximum force applied was 3 nN. In this case, 20 different cells were analyzed. On each cell, 126 force-distance curves were taken in a rectangular region of the somata. After taking each individual force-distance curve, the tip was displaced laterally about 10 μm. The Young's modulus was obtained by fitting a repulsive section of the force-distance curve with a bottom effect correction model for a spherical tip.[6,7] Embryonic neural progenitor cells for AFM testing of individual neural cells were gently provided by the *Hospital Nacional de Parapléjicos* (Toledo, Spain).

Magnetic resonance image (MRI) studies: Immediately after the perfusion-fixation procedure and the subsequent spinal cord extraction, the fragment between C4 and T1, which contains the main spinal cord structures involved in the rat anterior limb function, was cut under a magnifying glass and left overnight in paraformaldehyde (4 %). Afterwards, the tissue was washed several washes with 0.1 M phosphate buffer and placed inside a glass vial already filled in with Fluorinert medium, which was carefully sealed avoiding bubbles with parafilm. MRI images were acquired in a 7T Bruker Biospin MRI machine (Ettlingen, Germany) BioSpec 70/30. The different measurements were made using images of a turbo spin echo sequence enhanced in T2 (RARE turbo) and axial acquisition. The lesion/scaffold dimensions, their volume and

the presence of malacia/mass effect in the SCI epicenter were analyzed, as well as the number, location, size and MRI image intensity of the non-primarily damaged areas rostral and caudal to the SCI epicenter. Once the images were obtained, the spinal cord tissue was extracted from the glass vial, washed repeatedly with phosphate buffer to eliminate the Fluorinert medium and used for histological and immunofluorescence studies.
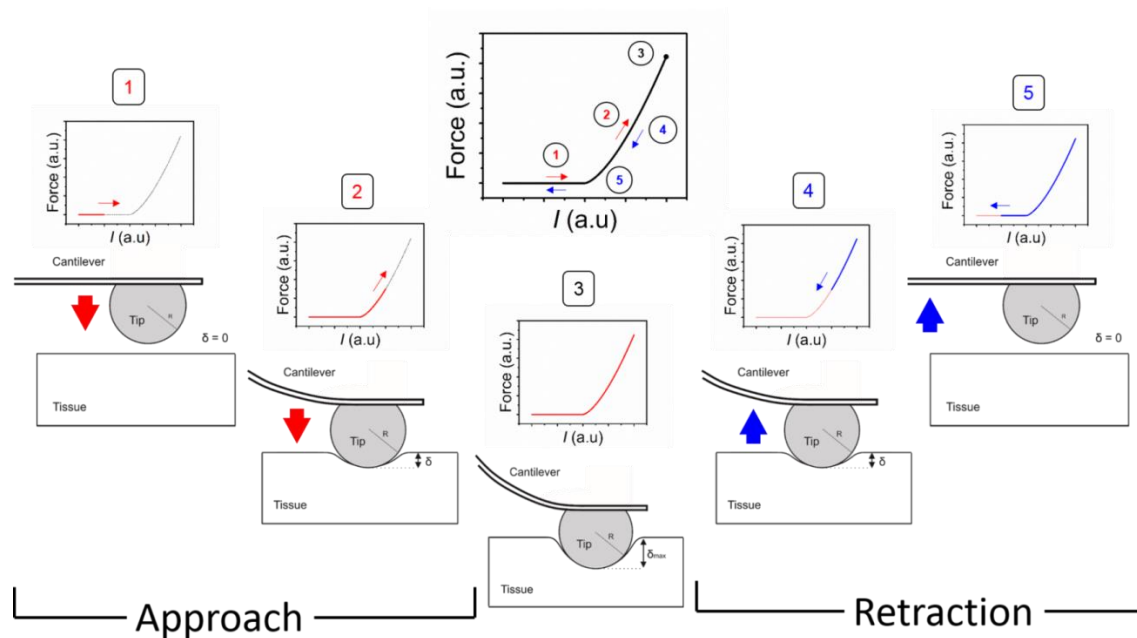
Supplementary figures

Figure S1. Scheme of a typical force-distance curve experiment. The force-distance curve has two sections, approach and retraction. In the approach, the cantilever moves toward the sample and indents it until a given force is reached (steps 1-3). In the retraction section, the tip moves away from the sample (steps 4-5). Red and blue colors refer to the approach and the retraction sections of the force-distance curve, respectively.
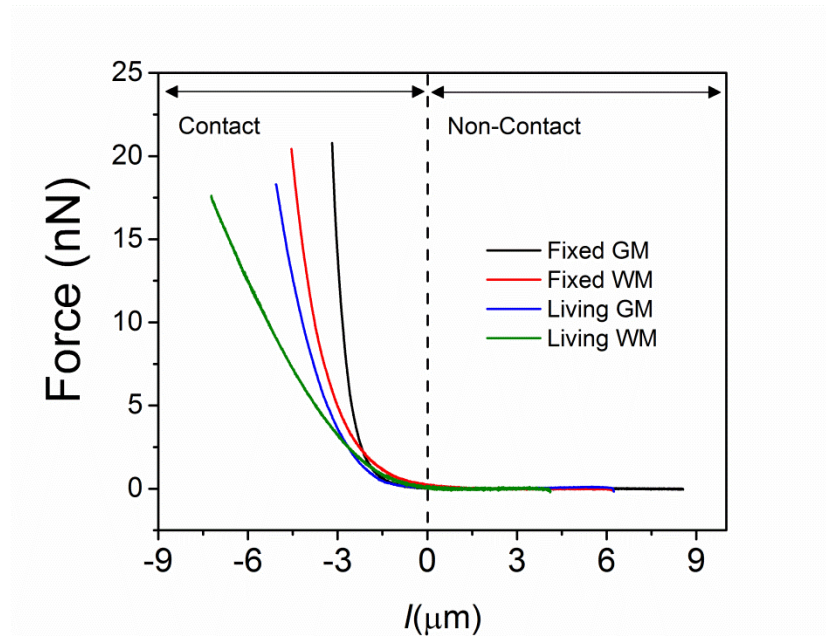
Figure S2. Force-distance curves obtained on spinal cord slices. The tip was approached towards the sample until a force of 20 nN was detected. The figure shows that the maximum indentation is sample dependent. This reflects the different Young's moduli of the different types of tissues. The data has been taken with the same cantilever-tip system. For the fixed spinal cord tissue, the grey matter is indented around 3 μm and the white matter 4.5 μm. The living spinal cord tissue is softer, with the maximum indentations reaching values of 5 μm (grey matter) and ~7.5 μm (white matter).
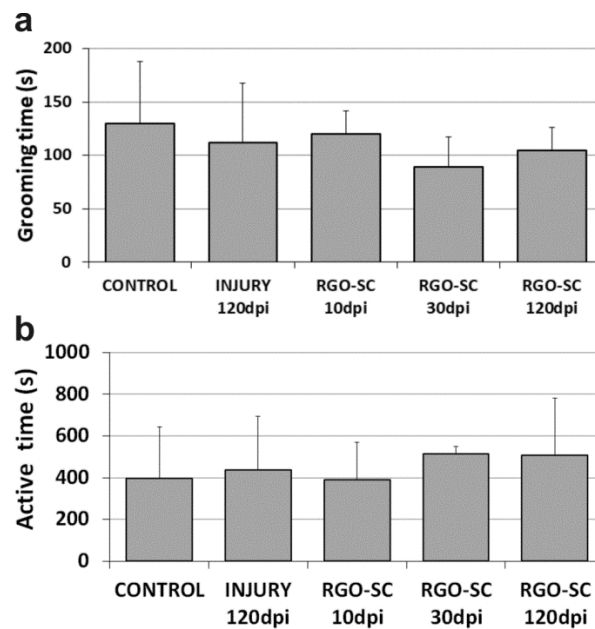

Figure S3. Active time during grooming (a) and asymmetry (b) behavioral tests in the different treatment groups (expressed in seconds).
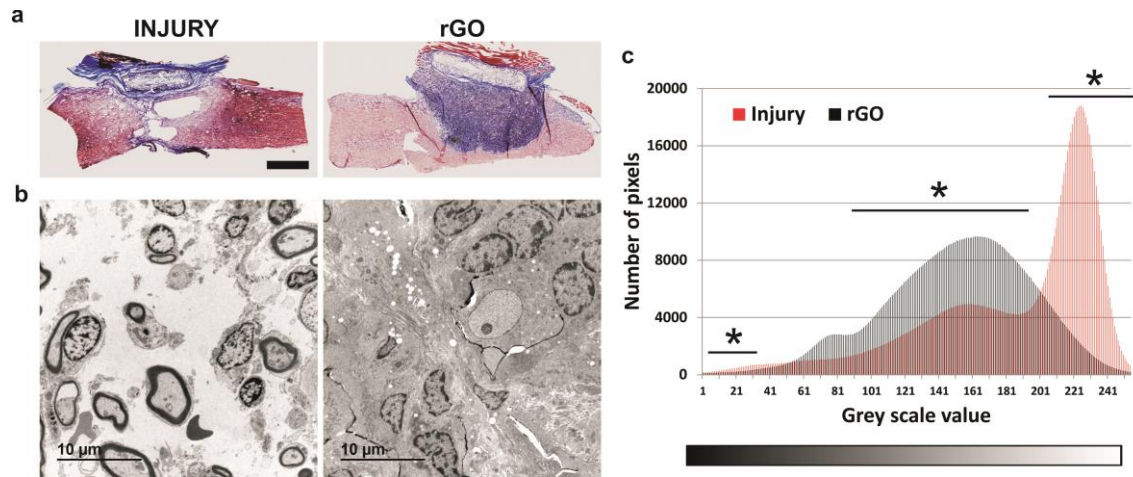
Figure S4. Representative spinal cord sections stained for collagen (a) from *I* and rGO rats. Scale bar: 1 mm. Representative TEM images illustrating the lesion site in *I* and rGO rats (b). Scale bars: 10 μm. Pseudo-quantitative estimations of the organization degree at the lesion site in *I* and rGO rats by analyses of variations in the grey-scale values of the images (c). Statistical comparisons: * p < 0.05.
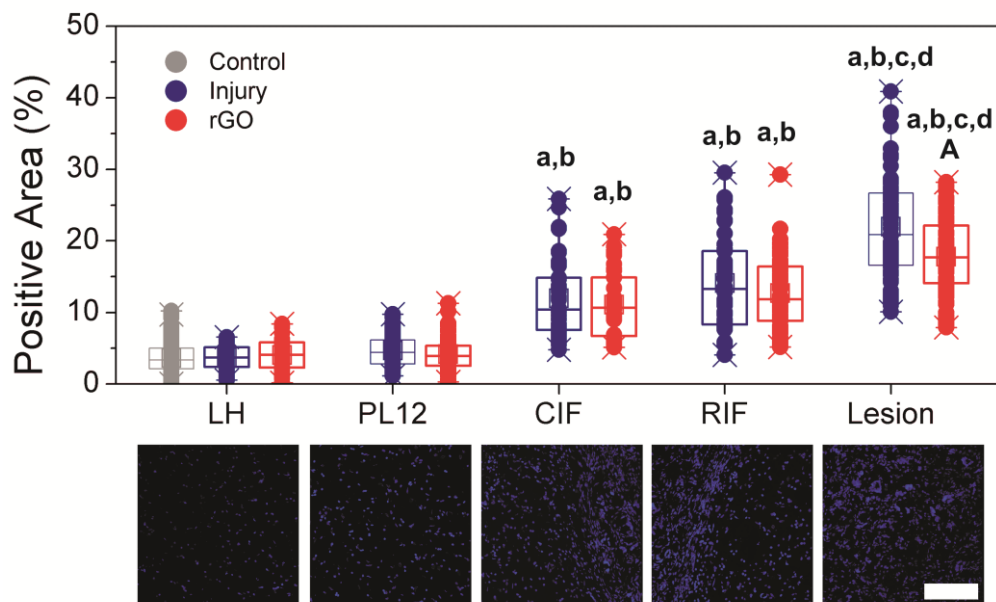

Figure S5. Cell density on the different areas under study in rGO rats as measured by Hoechst staining and CLSM. Control and injured rats without scaffolds are shown for comparisons. CIF: caudal interface; LH: left hemicord; PL12: perilesional areas at 1-2 mm from the lesion border; RIF: rostral interface. Scale bar: 150 μm. Statistics: significant differences with respect to (a) LH, (b) PL12, (c) CIF, (d) RIF, and (A) *I* group (p < 0.05).
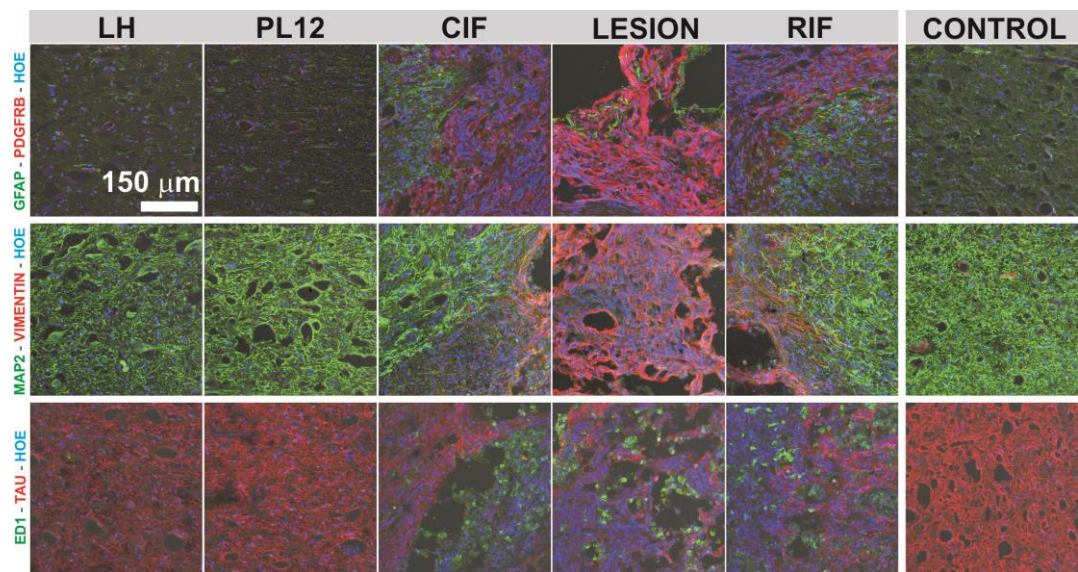
Figure S6. Representative immunofluorescence images for control (right) and injured rats without rGO scaffolds (left) at the different areas under study and the diverse markers analyzed. CIF: caudal interface; LH: left hemicord; PL12: perilesional areas at 1-2 mm from the lesion border; RIF: rostral interface. Scale bar: 150 μm.
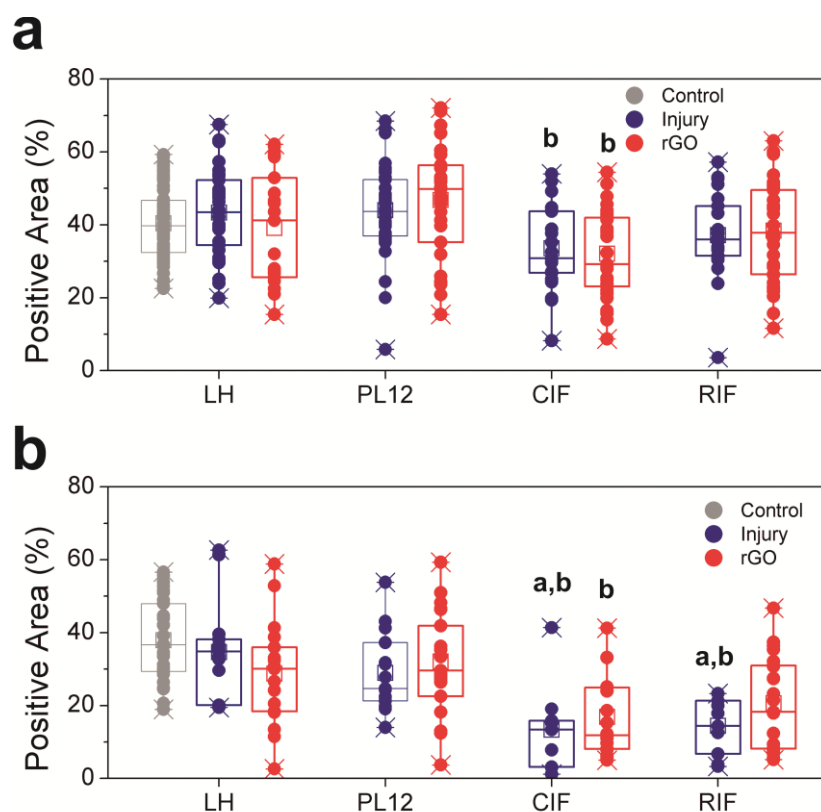

Figure S7. Neurite density at the different areas around the lesion site. Quantitative data from immunofluorescence images for β-III tubulin (a) and SMI311 (b). Values for control and injured rats without scaffolds are shown for comparison. Data are expressed as the mean ± standard deviation. CIF: caudal interface; LH: left hemicord; PL12: perilesional areas at 1-2 mm from the lesion border; RIF: rostral interface. Statistics: significant differences with respect to (a) LH and (b) PL12 ($p < 0.05$).
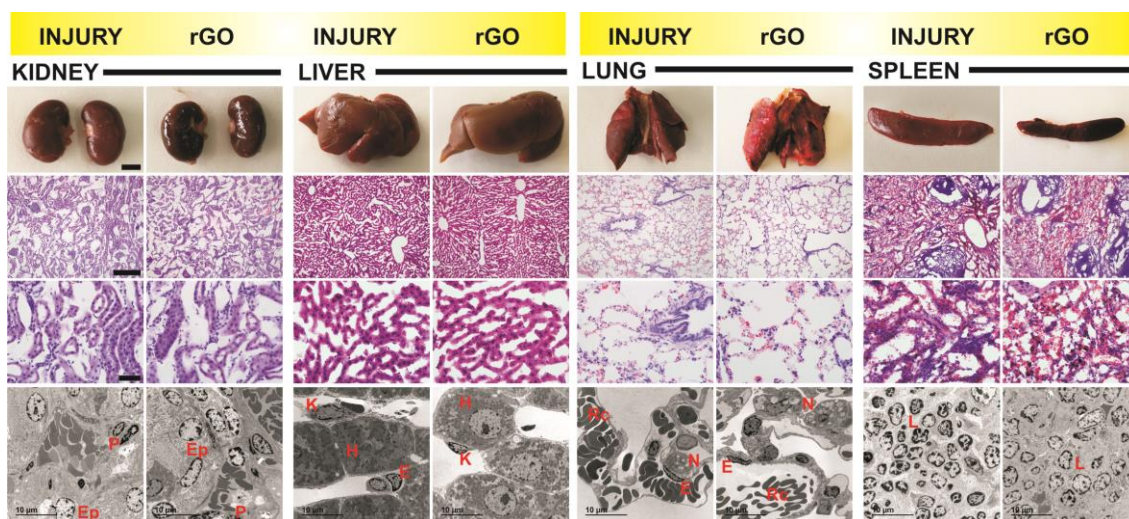
Figure S8. Histopathological and tissue structural effects of 4-month rGO scaffold implantation in key organs (kidneys, liver, lungs and spleen). Representative images from macroscopic views (top), H&E staining (middle) and TEM analyses (bottom). Scale bars: 2 mm, 250 μm, 50 μm, and 10 μm, respectively. Images from organs in rats without rGO scaffolds are shown for comparison. E: endothelial cell; Ep: epithelial cell; H: hepatocyte; K: Kuffer cell; L: lymphocytes; N: neumocyte; P: podocyte; Rc: red blood cell.

Table S1. Relative percentage of peak areas for each type of atomic bonding obtained by XPS C1s analysis of the studied samples and their correspondent O/C atomic ratio.

Sample	C sp2	C-C/H	C-OH	O-C-O	O-C=O	π-π*	O/C (at)
GO slurry	-	44.0	40.1	10.1	5.8	-	0.84
GO scaffold	39.9	9.3	30.1	10.7	8.3	1.7	0.38
rGO scaffold	57.5	14.9	15.1	1.8	8.7	2.0	0.28

Table S2. Summary of antibodies used for immunofluorescence studies.

Antibody	Supplier	Catalog Number	Dilution
Anti-MAP2	Sigma-Aldrich	M1406	1:500
Anti-Vimentin	Sigma-Aldrich	SAB4300676	1:500
Anti-Glial fibrillary acidic protein	Sigma-Aldrich	G3893	1:400
Anti-Platelet derived growth factor receptor β	Abcam	ab32570	1:100
Anti-Neurofilament marker (pan-neuronal, cocktail) (Previously Covance SMI-311R)	BioLegend	837802	1:500
Anti-β-III Tubulin	Sigma-Aldrich	T2200	1:500
Anti-Laminin	LSBio	LS-C96142	1:500
Anti-RECA-1	Bio-Rad	MCA970R	1:250
Anti-vGlut2	Synaptic Sytems	135 403	1:500
Anti-Tyrosine hydroxylase	Abcam	ab76442	1:250

References

[1] F. Della Pellea, R. Di Battistaa, L. Vázquez, F. J. Palomares, M. Del Carlo, M. Sergi, D. Compagnone, A. Escarpa, *Appl. Mater. Today* **2017**, *9*, 29.

[2] J. A. Bertelli, J. C. Mira, *J. Neurosci. Methods* **1993**, *46*, 203.

[3] J. C. Gensel, C. A. Tovar, F. P. T. Hamers, R. J. Deibert, M. S. Beattie, J. Bresnahan, *J. Neurotrauma* **2006**, *23*, 36.

[4] T. Schallert, S. M. Fleming, J. L. Leasure, J. L. Tillerson, S. T. Bland, *Neuropharmacology* **2000**, *39*, 777.

[5] J. S. Soblosky, J. H. Song, D. H. Dinh, *Behav. Brain Res.* **2001**, *119*, 1.

[6] P. D. Garcia, R. Garcia, *Biophys. J.* **2018**, *114*, 2923.

[7] P. D. Garcia, C. R. Guerrero, R. Garcia, *Nanoscale* **2017**, *9*, 12051.